

$\Lambda_c \rightarrow N$ form factors from lattice QCD and phenomenology of $\Lambda_c \rightarrow n \ell^+ \nu_\ell$ and $\Lambda_c \rightarrow p \mu^+ \mu^-$ decays

Stefan Meinel

*Department of Physics, University of Arizona, Tucson, AZ 85721, USA and
RIKEN BNL Research Center, Brookhaven National Laboratory, Upton, NY 11973, USA*

A lattice QCD determination of the $\Lambda_c \rightarrow N$ vector, axial vector, and tensor form factors is reported. The calculation was performed with $2 + 1$ flavors of domain wall fermions at lattice spacings of $a \approx 0.11$ fm, 0.085 fm and pion masses in the range $230 \text{ MeV} \lesssim m_\pi \lesssim 350 \text{ MeV}$. The form factors are extrapolated to the continuum limit and the physical pion mass using modified z expansions. The rates of the charged-current decays $\Lambda_c \rightarrow n e^+ \nu_e$ and $\Lambda_c \rightarrow n \mu^+ \nu_\mu$ are predicted to be $(0.405 \pm 0.016_{\text{stat}} \pm 0.020_{\text{syst}}) |V_{cd}|^2 \text{ ps}^{-1}$ and $(0.396 \pm 0.016_{\text{stat}} \pm 0.020_{\text{syst}}) |V_{cd}|^2 \text{ ps}^{-1}$, respectively. The phenomenology of the rare charm decay $\Lambda_c \rightarrow p \mu^+ \mu^-$ is also studied. The differential branching fraction, the fraction of longitudinally polarized dimuons, and the forward-backward asymmetry are calculated in the Standard Model and in an illustrative new-physics scenario.

I. INTRODUCTION

This paper reports a lattice QCD calculation of the form factors describing the matrix elements $\langle N | \bar{q} \Gamma c | \Lambda_c \rangle$, where q denotes the up or down quark field, N denotes the proton or neutron, and $\Gamma \in \{\gamma^\mu, \gamma^\mu \gamma_5, \sigma_{\mu\nu}\}$. The calculation was done in the isospin-symmetric limit with $m_u = m_d$, in which the $\Lambda_c \rightarrow n$ and $\Lambda_c \rightarrow p$ form factors are exactly equal: $\langle n | \bar{d} \Gamma c | \Lambda_c \rangle = \langle p | \bar{u} \Gamma c | \Lambda_c \rangle$. The $\Lambda_c \rightarrow n$ vector and axial vector form factors govern the charged-current decays $\Lambda_c \rightarrow n \ell^+ \nu_\ell$, whose rates are proportional to $|V_{cd}|^2$. While the combination of a neutron and a neutrino in the final state makes measurements of these processes difficult, a precise first-principles calculation is still valuable, primarily to test other theoretical approaches [1–8]. The $\Lambda_c \rightarrow p$ form factors play a role in the rare charm decays $\Lambda_c \rightarrow p \ell^+ \ell^-$, $\Lambda_c \rightarrow p \gamma$, and others. Rare charm decays provide an opportunity to search for new fundamental physics, but this is more challenging than in the bottom sector due to the dominance of long-distance contributions from nonlocal matrix elements in most or all of the kinematic range (except for some observables that vanish in the Standard Model). Recent theoretical studies of mesonic rare charm decays such as $D^+ \rightarrow \pi^+ \mu^+ \mu^-$ can be found in Refs. [9–11]. This work focuses on the decay $\Lambda_c \rightarrow p \mu^+ \mu^-$, which was recently analyzed by the LHCb Collaboration [12]. In the dimuon mass region excluding ± 40 MeV intervals around m_ω and m_ϕ , an upper limit of $\mathcal{B}(\Lambda_c \rightarrow p \mu^+ \mu^-) < 7.7 \times 10^{-8}$ at 90% confidence level was obtained [12], which is a substantial improvement over previous limits set by the BaBar [13] and Fermilab E653 [14] Collaborations.

The remainder of the paper is structured as follows: The form factors are defined in Sec. II. The lattice QCD calculation is described in Sec. III. The predictions for the $\Lambda_c \rightarrow n e^+ \nu_e$ and $\Lambda_c \rightarrow n \mu^+ \nu_\mu$ decay rates are presented in Sec. IV, and the rare decay $\Lambda_c \rightarrow p \mu^+ \mu^-$ is analyzed in Sec. V. Conclusions are given in Sec. VI.

II. DEFINITION OF THE FORM FACTORS

In the following, we consider the proton final state for definiteness. This calculation uses the helicity-based definition of the form factors introduced in Ref. [15], which is given by

$$\begin{aligned} \langle N^+(p', s') | \bar{u} \gamma^\mu c | \Lambda_c(p, s) \rangle &= \bar{u}_N(p', s') \left[f_0(q^2) (m_{\Lambda_c} - m_N) \frac{q^\mu}{q^2} \right. \\ &\quad + f_+(q^2) \frac{m_{\Lambda_c} + m_N}{s_+} \left(p^\mu + p'^\mu - (m_{\Lambda_c}^2 - m_N^2) \frac{q^\mu}{q^2} \right) \\ &\quad \left. + f_\perp(q^2) \left(\gamma^\mu - \frac{2m_N}{s_+} p^\mu - \frac{2m_{\Lambda_c}}{s_+} p'^\mu \right) \right] u_{\Lambda_c}(p, s), \end{aligned} \quad (1)$$

$$\begin{aligned} \langle N^+(p', s') | \bar{u} \gamma^\mu \gamma_5 c | \Lambda_c(p, s) \rangle &= -\bar{u}_N(p', s') \gamma_5 \left[g_0(q^2) (m_{\Lambda_c} + m_N) \frac{q^\mu}{q^2} \right. \\ &\quad + g_+(q^2) \frac{m_{\Lambda_c} - m_N}{s_-} \left(p^\mu + p'^\mu - (m_{\Lambda_c}^2 - m_N^2) \frac{q^\mu}{q^2} \right) \\ &\quad \left. + g_\perp(q^2) \left(\gamma^\mu + \frac{2m_N}{s_-} p^\mu - \frac{2m_{\Lambda_c}}{s_-} p'^\mu \right) \right] u_{\Lambda_c}(p, s), \end{aligned} \quad (2)$$

$$\begin{aligned} \langle N^+(p', s') | \bar{u} i\sigma^{\mu\nu} q_\nu c | \Lambda_c(p, s) \rangle = & -\bar{u}_N(p', s') \left[h_+(q^2) \frac{q^2}{s_+} \left(p^\mu + p'^\mu - (m_{\Lambda_c}^2 - m_\Lambda^2) \frac{q^\mu}{q^2} \right) \right. \\ & \left. + h_\perp(q^2) (m_{\Lambda_c} + m_N) \left(\gamma^\mu - \frac{2m_N}{s_+} p^\mu - \frac{2m_{\Lambda_c}}{s_+} p'^\mu \right) \right] u_{\Lambda_c}(p, s), \end{aligned} \quad (3)$$

$$\begin{aligned} \langle N^+(p', s') | \bar{u} i\sigma^{\mu\nu} q_\nu \gamma_5 c | \Lambda_c(p, s) \rangle = & -\bar{u}_\Lambda(p', s') \gamma_5 \left[\tilde{h}_+(q^2) \frac{q^2}{s_-} \left(p^\mu + p'^\mu - (m_{\Lambda_c}^2 - m_\Lambda^2) \frac{q^\mu}{q^2} \right) \right. \\ & \left. + \tilde{h}_\perp(q^2) (m_{\Lambda_c} - m_N) \left(\gamma^\mu + \frac{2m_N}{s_-} p^\mu - \frac{2m_{\Lambda_c}}{s_-} p'^\mu \right) \right] u_{\Lambda_c}(p, s), \end{aligned} \quad (4)$$

where $q = p - p'$, $\sigma^{\mu\nu} = \frac{i}{2}(\gamma^\mu\gamma^\nu - \gamma^\nu\gamma^\mu)$, and $s_\pm = (m_{\Lambda_c} \pm m_N)^2 - q^2$. These form factors satisfy the endpoint relations

$$f_0(0) = f_+(0), \quad (5)$$

$$g_0(0) = g_+(0), \quad (6)$$

$$g_\perp(q_{\max}^2) = g_+(q_{\max}^2), \quad (7)$$

$$\tilde{h}_\perp(q_{\max}^2) = \tilde{h}_+(q_{\max}^2), \quad (8)$$

where $q_{\max}^2 = (m_{\Lambda_c} - m_N)^2$.

III. LATTICE CALCULATION

A. Lattice parameters and correlation functions

This calculation uses the Iwasaki action [16] for the gluons, the Shamir-type domain-wall action [17–19] for the u , d , and s quarks, and an anisotropic clover action for the c quark, with parameters tuned in Ref. [20] to reproduce the correct charmonium mass and relativistic dispersion relation. The gauge field ensembles were generated by the RBC and UKQCD Collaborations and are described in detail in Ref. [21]. This work is based on the same six sets of light-quark domain-wall propagators as Ref. [22]; the parameters of these sets and the resulting pion masses are listed in Table I. The parameters of the charm-quark action are given in the first four rows of Table II.

The Λ_c and nucleon two-point functions and the $\Lambda_c \rightarrow N$ three-point functions were computed analogously to Ref. [22], with the bottom quark replaced by the charm quark. The $c \rightarrow u$ currents were renormalized using the “mostly nonperturbative” method [24, 25], in which the bulk of the renormalization is absorbed by an overall factor of $\sqrt{Z_V^{(uu)} Z_V^{(cc)}}$, where $Z_V^{(uu)}$ and $Z_V^{(cc)}$ are the nonperturbative renormalization factors of the currents $\bar{u}\gamma_0 u$ and $\bar{c}\gamma_0 c$. The $c \rightarrow u$ vector and axial vector currents are defined as in Eqs. (18)-(21) of Ref. [22], with residual matching factors and $\mathcal{O}(a)$ -improvement coefficients computed to one loop by Christoph Lehner [26, 27] and listed in Table II. The full one-loop $\mathcal{O}(a)$ improvement was performed for the vector and axial vector currents for all source-sink separations in the three-point functions (instead of just a subset of separations as in Ref. [22]). For the $c \rightarrow u$ tensor currents, the one-loop calculation was not available, and the perturbative coefficients were evaluated at tree-level as in Ref. [28]. That is, the tensor currents were written as

$$T_{\mu\nu} = \sqrt{Z_V^{(uu)} Z_V^{(cc)}} \left[\bar{u} \sigma_{\mu\nu} c + a d_1 \sum_{j=1}^3 \bar{u} \sigma_{\mu\nu} \gamma_j \vec{\nabla}_j c \right], \quad (9)$$

Set	β	$N_s^3 \times N_t$	$am_{u,d}^{(\text{sea})}$	$am_s^{(\text{sea})}$	a [fm]	$am_{u,d}^{(\text{val})}$	$m_\pi^{(\text{val})}$ [MeV]	N_{samples}
C14	2.13	$24^3 \times 64$	0.005	0.04	0.1119(17)	0.001	245(4)	2672
C24	2.13	$24^3 \times 64$	0.005	0.04	0.1119(17)	0.002	270(4)	2676
C54	2.13	$24^3 \times 64$	0.005	0.04	0.1119(17)	0.005	336(5)	2782
F23	2.25	$32^3 \times 64$	0.004	0.03	0.0849(12)	0.002	227(3)	1907
F43	2.25	$32^3 \times 64$	0.004	0.03	0.0849(12)	0.004	295(4)	1917
F63	2.25	$32^3 \times 64$	0.006	0.03	0.0848(17)	0.006	352(7)	2782

TABLE I. Parameters of the lattice gauge field ensembles [21] and light quark propagators. The C14/C24 and F23 data sets are based on the same gauge field ensembles as the C54 and F43 data sets, respectively, and differ only in the valence quark mass used for the propagators. The lattice spacing values given here were determined using the $\Upsilon(2S) - \Upsilon(1S)$ splitting in Ref. [23].

Parameter	Coarse lattice	Fine lattice
am_c	0.1214	-0.0045
ν	1.2362	1.1281
c_E	1.6650	1.5311
c_B	1.8409	1.6232
d_1	0.0437	0.0355
$Z_V^{(cc)}$	1.35725(23)	1.18321(14)
$Z_V^{(uu)}$	0.71651(46)	0.74475(12)
$\rho_{V^0} = \rho_{A^0}$	1.00274(49)	1.001949(85)
$\rho_{V^j} = \rho_{A^j}$	0.99475(62)	0.99675(68)
$c_{V^0}^R = c_{A^0}^R$	0.0402(88)	0.0353(92)
$c_{V^0}^L = c_{A^0}^L$	-0.0048(48)	-0.0027(28)
$c_{V^j}^R = c_{A^j}^R$	0.0346(51)	0.0283(43)
$c_{V^j}^L = c_{A^j}^L$	0.00012(26)	0.00040(42)
$d_{V^j}^R = -d_{A^j}^R$	-0.0041(41)	-0.0039(39)
$d_{V^j}^L = -d_{A^j}^L$	0.0021(21)	0.0026(26)

TABLE II. Charm-quark action parameters [20] and $c \rightarrow u$ current matching and $\mathcal{O}(a)$ improvement parameters [26, 27]. The nonperturbative factors $Z_V^{(uu)}$ and $Z_V^{(cc)}$ were determined in Refs. [30] and [22], respectively. The uncertainties of the residual matching factors and $\mathcal{O}(a)$ -improvement coefficients were estimated as $(h^{(0)}/h^{(1)} - 1)^2 h^{(1)}$, where $h^{(0)}$ is the tree-level result and $h^{(1)}$ is the full one-loop result [26, 27].

Set	am_{Λ_c}	am_N	am_D
C14	1.3499(51)	0.6184(76)	1.0728(12)
C24	1.3526(57)	0.6259(57)	1.0713(14)
C54	1.3706(40)	0.6580(39)	1.0763(13)
F23	1.008(12)	0.4510(86)	0.8092(11)
F43	1.0185(67)	0.4705(42)	0.81185(91)
F63	1.0314(40)	0.5004(25)	0.81722(56)

TABLE III. Hadron masses in lattice units.

where d_1 is the mean-field-improved heavy-quark ‘‘field rotation’’ coefficient [29], whose values are also listed in Table II. The missing one-loop corrections result in larger systematic uncertainties for the tensor form factors, as discussed in Sec. III B.

The three-point functions were computed for all source-sink separations in the ranges $t/a = 4..15$ (C14, C24, C54 data sets), $t/a = 5..15$ (F43 data set), and $t/a = 5..17$ (F63 data set). The Λ_c momentum, \mathbf{p} , was set to zero, and all nucleon momenta \mathbf{p}' with $1 \left(\frac{2\pi}{L}\right)^2 \leq |\mathbf{p}'|^2 \leq 5 \left(\frac{2\pi}{L}\right)^2$ were used. From the three-point and two-point correlation functions, the ‘‘ratios’’ $R_{f_\perp}(|\mathbf{p}'|, t)$, $R_{f_+}(|\mathbf{p}'|, t)$, $R_{f_0}(|\mathbf{p}'|, t)$, $R_{g_\perp}(|\mathbf{p}'|, t)$, $R_{g_+}(|\mathbf{p}'|, t)$, $R_{g_0}(|\mathbf{p}'|, t)$, $R_{h_\perp}(|\mathbf{p}'|, t)$, $R_{h_+}(|\mathbf{p}'|, t)$, $R_{\tilde{h}_\perp}(|\mathbf{p}'|, t)$, and $R_{\tilde{h}_+}(|\mathbf{p}'|, t)$, defined as in Eqs. (52-54), (58-60) of Ref. [22] and Eqs. (27-30) of Ref. [28] (with the appropriate replacements of initial and final baryons), were computed. These ratios are equal to the form factors f_\perp, f_+, \dots for the given momentum and lattice parameters, up to excited-state contributions that vanish exponentially as $t \rightarrow \infty$. The ratios also depend on the baryon masses, which were obtained by fitting the two-point functions from the same data sets and are listed in Table III (the table also contains the D meson masses, which are needed at a later stage in the analysis).

The ground-state form factors $f(|\mathbf{p}'|)$ were then extracted by performing correlated fits of the ratios of the form $R_f(|\mathbf{p}'|, t) = f(|\mathbf{p}'|) + A_f(|\mathbf{p}'|) e^{-\delta_f(|\mathbf{p}'|)t}$, which include the leading excited-state contributions. Examples of the fits are shown in Fig. 1. At a given momentum, the fits were performed jointly for all six data sets, and jointly for the form factors associated with a given type of current, with constraints as explained in Ref. [22]. The constraints limit the variation of the energy gap parameters across data sets to physically reasonable values, and enforce that the relations between the form factors in the helicity basis and the ‘‘Weinberg basis’’ are preserved by the extrapolation [22, 28].

The values of the start time slices t_{\min} were chosen to achieve $\chi^2/\text{d.o.f.} \lesssim 1$. The average of the $\chi^2/\text{d.o.f.}$ values of

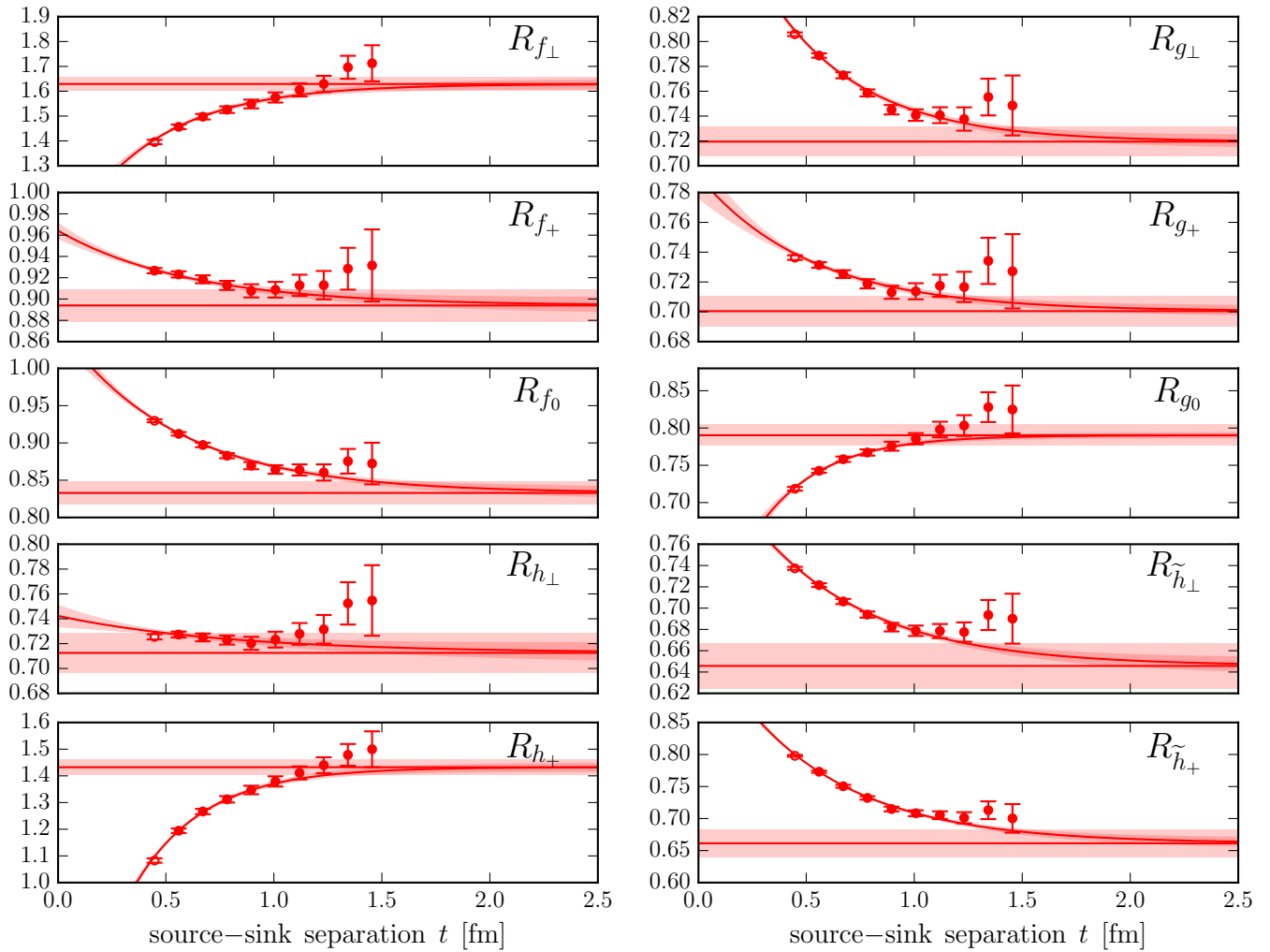


FIG. 1. Fits of the quantities $R_f(|\mathbf{p}'|, t)$ that are used to extract the ground-state form factors, $f(|\mathbf{p}'|) = \lim_{t \rightarrow \infty} R_f(|\mathbf{p}'|, t)$. The data shown here are from the C54 set at $|\mathbf{p}'|^2 = 2 \left(\frac{2\pi}{L}\right)^2$. At a given momentum, the fits were performed jointly for all six data sets with constraints as explained in Ref. [22]. Some data points at the shortest source-sink separations, plotted with open symbols, were excluded from the fits to achieve $\chi^2/\text{d.o.f.} \lesssim 1$. The curves going through the data points show the fit functions of the form $R_f(|\mathbf{p}'|, t) = f(|\mathbf{p}'|) + A_f(|\mathbf{p}'|) e^{-\delta_f(|\mathbf{p}'|)t}$, with bands giving the statistical uncertainties. The horizontal lines show the extrapolated values $f(|\mathbf{p}'|)$, where the bands also include estimates of the systematic uncertainties associated with the choices of fit ranges.

the twenty independent fits (four types of currents times five momenta) was 0.98, with a standard deviation of 0.16. The number of degrees of freedom (d.o.f.), defined as the number of data points minus the number of unconstrained fit parameters, ranged from 94 to 294. The average and standard deviation of the magnitudes $|A_f(|\mathbf{p}'|)|$ of the excited-state-overlap parameters were 0.56 ± 0.73 for the form factors in the helicity basis and 0.78 ± 1.05 for the form factors in the Weinberg basis.

To estimate the remaining systematic uncertainties associated with the choices of fit ranges, additional fits were performed in which all t_{\min} values were increased simultaneously by one unit. As in Refs. [22, 28, 31], the systematic uncertainty in $f(|\mathbf{p}'|)$ for a given momentum $|\mathbf{p}'|$ and data set was estimated as the larger of the following two: i) the shift in $f(|\mathbf{p}'|)$ at the given momentum, and ii) the average of the shifts in $f(|\mathbf{p}'|)$ over all momenta. These systematic uncertainties were added to the statistical uncertainties in quadrature. The results for $f(|\mathbf{p}'|)$ with the combined uncertainties are listed in Table VIII in the Appendix, and are also shown as the horizontal bands in Fig. 1 and as the data points in Figs. 2-4.

B. Chiral and continuum extrapolations of the form factors

Following the extraction of the form factor values for each lattice data set and for each discrete momentum, global fits of the form factor shape and of the dependence on the lattice spacing and quark masses were performed using modified BCL z -expansions [32]. In the physical limit ($a = 0$, $m_\pi = m_{\pi,\text{phys}}$), the fit functions reduce to the form

$$f(q^2) = \frac{1}{1 - q^2/(m_{\text{pole}}^f)^2} \sum_{n=0}^{n_{\text{max}}} a_n^f [z(q^2)]^n, \quad (10)$$

where the expansion variable is defined as

$$z(q^2) = \frac{\sqrt{t_+ - q^2} - \sqrt{t_+ - t_0}}{\sqrt{t_+ - q^2} + \sqrt{t_+ - t_0}}. \quad (11)$$

This definition maps the complex q^2 plane, cut along the real axis for $q^2 \geq t_+$, onto the disk $|z| < 1$. Here, t_+ is set equal to the threshold of $D\pi$ two-particle states,

$$t_+ = (m_D + m_\pi)^2. \quad (12)$$

The parameter t_0 determines which value of q^2 gets mapped to $z = 0$; in this work,

$$t_0 = q_{\text{max}}^2 = (m_{\Lambda_c} - m_N)^2 \quad (13)$$

is used. Furthermore, in Eq. (10), the lowest poles are factored out before the z expansion. The quantum numbers and masses of the D mesons producing these poles in the different form factors are given in Table IV.

To fit the lattice data, Eq. (10) was augmented with additional parameters to describe the dependence on the lattice spacing and on m_π^2 (which serves as a proxy for the u/d quark mass). As in Refs. [22, 28], two independent fits were performed: a ‘‘nominal’’ fit, which provides the central values and statistical uncertainties of the form factors, and a ‘‘higher-order (HO)’’ fit that is used to estimate systematic uncertainties. In this work, the functions used for the nominal fit were

$$f(q^2) = \frac{1}{1 - (a^2 q^2)/(am_D + a\Delta^f)^2} \left[a_0^f \left(1 + c_0^f \frac{m_\pi^2 - m_{\pi,\text{phys}}^2}{\Lambda_\chi^2} \right) + a_1^f z(q^2) + a_2^f [z(q^2)]^2 \right] \\ \times \left[1 + b^f a^2 |\mathbf{p}'|^2 + d^f a^2 \Lambda_{\text{had}}^2 \right], \quad (14)$$

with free parameters a_0^f , a_1^f , a_2^f , c_0^f , b^f , and d^f . Here, the scales $\Lambda_\chi = 4\pi f_\pi$ with $f_\pi = 132$ MeV and $\Lambda_{\text{had}} = 300$ MeV were introduced to make all parameters dimensionless. The momentum transfers in lattice units, $a^2 q^2$, were evaluated using the lattice results for the baryon masses from each data set, and their uncertainties and correlations were taken into account. In addition, the pole masses were rewritten as $am_{\text{pole}}^f = am_D + a\Delta^f$, where Δ^f are the mass differences relative to the pseudoscalar D meson. These mass differences were fixed to their physical values according to Table IV, while the lattice results from each data set were used to evaluate am_D .

The systematic uncertainties associated with the choices of t_{min} in the extractions of the lattice form factors from the ratios of correlation functions (cf. Sec. III A) were considered to be part of the statistical uncertainties in the z -expansion fits discussed here, and were therefore included in the data covariance matrix for both the nominal and higher-order fits. Given that the procedure for estimating these uncertainties was based on the magnitudes in the shifts, and conservatively used the larger of two choices, there is no obviously correct way of evaluating their correlations. These systematic uncertainties were therefore added to the diagonal elements of the covariance matrices only. As a result, the z -expansion fits have rather low values of $\chi^2/\text{d.o.f.}$ (0.20 for the nominal fit and 0.19 for the higher-order fit, with d.o.f. = 235).

The functions used for the higher-order fit were

$$f_{\text{HO}}(q^2) = \frac{1}{1 - (a^2 q^2)/(am_D + a\Delta^f)^2} \left[a_0^f \left(1 + c_0^f \frac{m_\pi^2 - m_{\pi,\text{phys}}^2}{\Lambda_\chi^2} + \tilde{c}_0^f \frac{m_\pi^3 - m_{\pi,\text{phys}}^3}{\Lambda_\chi^3} \right) \right. \\ \left. + a_1^f \left(1 + c_1^f \frac{m_\pi^2 - m_{\pi,\text{phys}}^2}{\Lambda_\chi^2} \right) z(q^2) + a_2^f [z(q^2)]^2 + a_3^f [z(q^2)]^3 \right] \\ \times \left[1 + b^f a^2 |\mathbf{p}'|^2 + d^f a^2 \Lambda_{\text{had}}^2 + \tilde{b}^f a^4 |\mathbf{p}'|^4 + \tilde{d}^f a^3 \Lambda_{\text{had}}^3 + \tilde{d}^f a^4 \Lambda_{\text{had}}^4 + j^f a^4 |\mathbf{p}'|^2 \Lambda_{\text{had}}^2 \right]. \quad (15)$$

f	J^P	m_{pole}^f [GeV]
$f_+, f_\perp, h_+, h_\perp$	1^-	2.010
f_0	0^+	2.351
$g_+, g_\perp, \tilde{h}_+, \tilde{h}_\perp$	1^+	2.423
g_0	0^-	1.870

TABLE IV. The quantum numbers and masses of the D mesons producing poles in the different form factors [34]. To evaluate t_+ , the values $m_D = 1.870$ GeV and $m_\pi = 135$ MeV should be used.

The nominal fit already provides a good description of the lattice data, and the additional terms in the higher-order fit are used only to estimate systematic uncertainties in a Bayesian approach. To this end, the additional parameters were constrained with Gaussian priors to be no larger than natural-sized. The priors for the parameters \tilde{c}_0^f , c_1^f , \tilde{b}^f , \tilde{d}^f , \tilde{d}^f , and j^f were chosen as in Ref. [28], while the a_3^f were constrained to be 0 ± 30 as in Ref. [31]. In the higher-order fit, additional sources of systematic uncertainties were simultaneously incorporated as follows:

1. When generating the bootstrap samples for the ratios $R_{f_\perp}(|\mathbf{p}'|, t)$, $R_{f_+}(|\mathbf{p}'|, t)$, $R_{f_0}(|\mathbf{p}'|, t)$, $R_{g_\perp}(|\mathbf{p}'|, t)$, $R_{g_+}(|\mathbf{p}'|, t)$, $R_{g_0}(|\mathbf{p}'|, t)$, the residual matching factors and $\mathcal{O}(a)$ -improvement coefficients were drawn from Gaussian random distributions with central values and widths according to Table II.
2. To incorporate the systematic uncertainty in the tensor form factors due to the use of the tree-level values $\rho_{T^{\mu\nu}} = 1$ for the residual matching factors, nuisance parameters $\rho_{T^{\mu\nu}}$ multiplying these form factors with Gaussian priors $1 \pm \sigma_{\rho_{T^{\mu\nu}}}$ were introduced in the fit. For the $b \rightarrow s$ currents in Ref. [28], $\sigma_{\rho_{T^{\mu\nu}}}$ was estimated to be equal to 2 times the maximum value of $|\rho_{V^\mu} - 1|$, $|\rho_{A^\mu} - 1|$, which was 0.05316, comparable in magnitude to actual one-loop results for $|\rho_{T^{\mu\nu}} - 1|$ obtained for staggered light quarks in Ref. [33]. For the $c \rightarrow u$ currents in this work, ρ_{V^μ} and ρ_{A^μ} are much closer to 1 (see Table II), and the analogous procedure would yield $\sigma_{\rho_{T^{\mu\nu}}} = 0.0105$. Given that the tensor current is scale-dependent and may exhibit qualitatively different behavior in a matching calculation (compared to the vector and axial vector currents), this appears to be too aggressive. The uncertainty estimate was therefore increased to $\sigma_{\rho_{T^{\mu\nu}}} = 0.05$, which is approximately 10 times the maximum value of $|\rho_{V^\mu} - 1|$, $|\rho_{A^\mu} - 1|$. This estimate of the uncertainty (and the numerical values of the tensor form factors) should be understood as corresponding to the scale $\mu = m_c$.
3. The finite-volume errors in the $\Lambda_c \rightarrow N$ form factors are expected to be approximately equal to those in the $\Lambda_b \rightarrow N$ form factors, which were estimated to be 3% for the parameters of this calculation [22]. The missing isospin breaking effects are expected to be of order $\mathcal{O}((m_d - m_u)/\Lambda_{\text{QCD}}) \approx 0.5\%$ and $\mathcal{O}(\alpha_{\text{e.m.}}) \approx 0.7\%$. The uncertainties from these sources were added to the data correlation matrix used in the fit.
4. The lattice spacings and pion masses of the different data sets were promoted to fit parameters, with Gaussian priors chosen according to their known central values and uncertainties.

In the physical limit, the nominal and higher-order fits reduce to the form given in Eq. (10), with $n_{\text{max}} = 2$ and $n_{\text{max}} = 3$, respectively. The solid curves in Figs. 2, 3, and 4 with shaded error bands show the form factors in the physical limit. The results for the relevant parameters are given in Table V. Files containing the parameter values and the full covariance matrices are provided as supplemental material [35]. The systematic uncertainty of any quantity depending on the form factors is estimated as

$$\sigma_{O, \text{syst}} = \max\left(|O_{\text{HO}} - O|, \sqrt{|\sigma_{O, \text{HO}}^2 - \sigma_O^2|}\right), \quad (16)$$

where O and O_{HO} are the central values obtained from the nominal and higher-order parameterizations, and σ_O and $\sigma_{O, \text{HO}}$ are the uncertainties propagated using the covariance matrices given in the supplemental material for the nominal and higher-order fit parameters. See also Ref. [28] for further explanations of this procedure.

A breakdown of the form factor systematic uncertainties into individual sources is shown in Fig. 5. This was obtained by performing additional fits to the lattice data where each one of the above modifications to the fit functions or data covariance matrix was done individually, and then comparing each of these fits to the nominal fit as in Eq. (16).

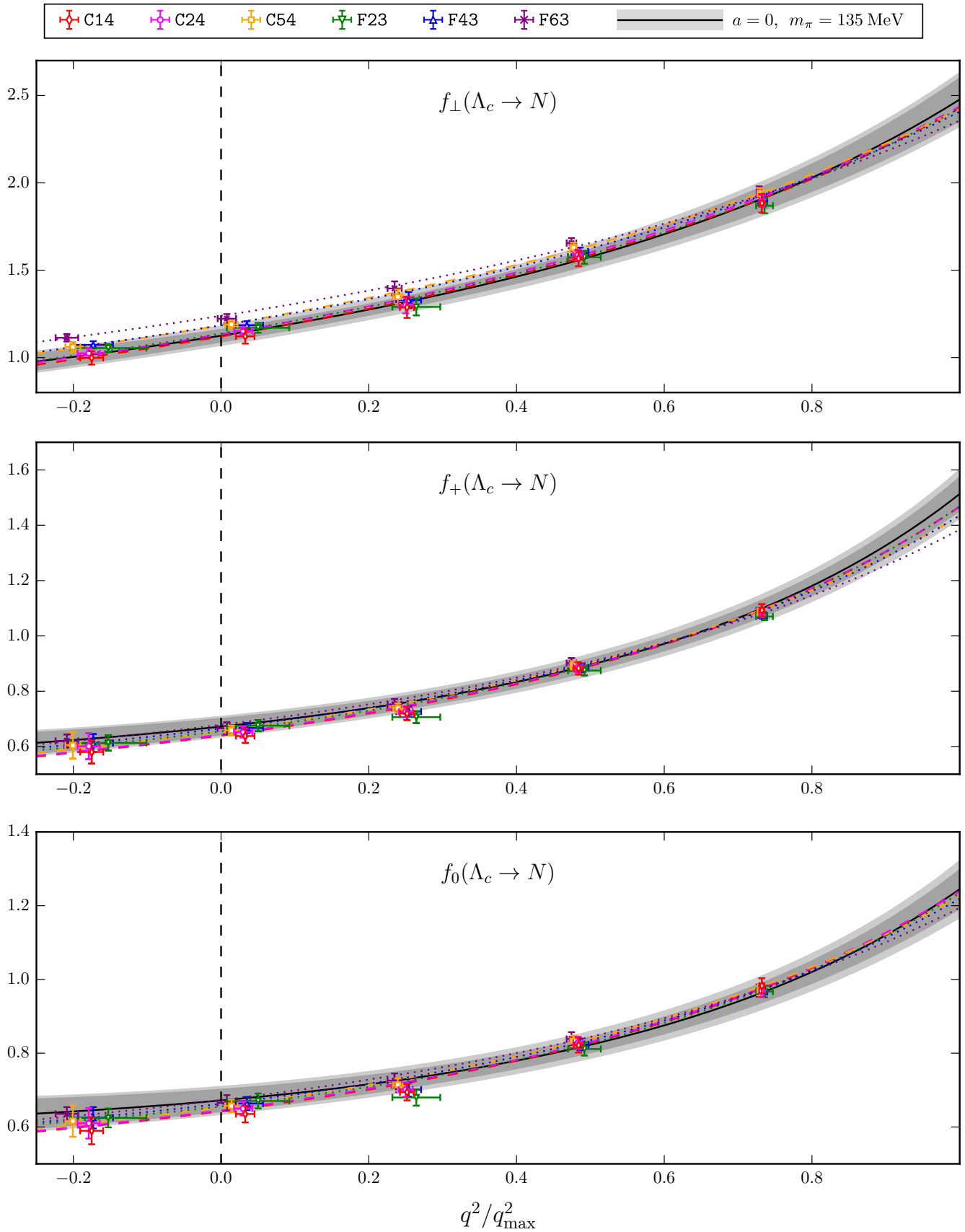


FIG. 2. Lattice QCD results for the $\Lambda_c \rightarrow N$ vector form factors from the six different data sets (the labels are explained in Table I), along with the modified z -expansion fits evaluated at the lattice parameters (dashed lines at $a \approx 0.11 \text{ fm}$ and dotted lines at $a \approx 0.085 \text{ fm}$) and in the physical limit (solid lines, with statistical and total uncertainties indicated by the inner and outer bands).

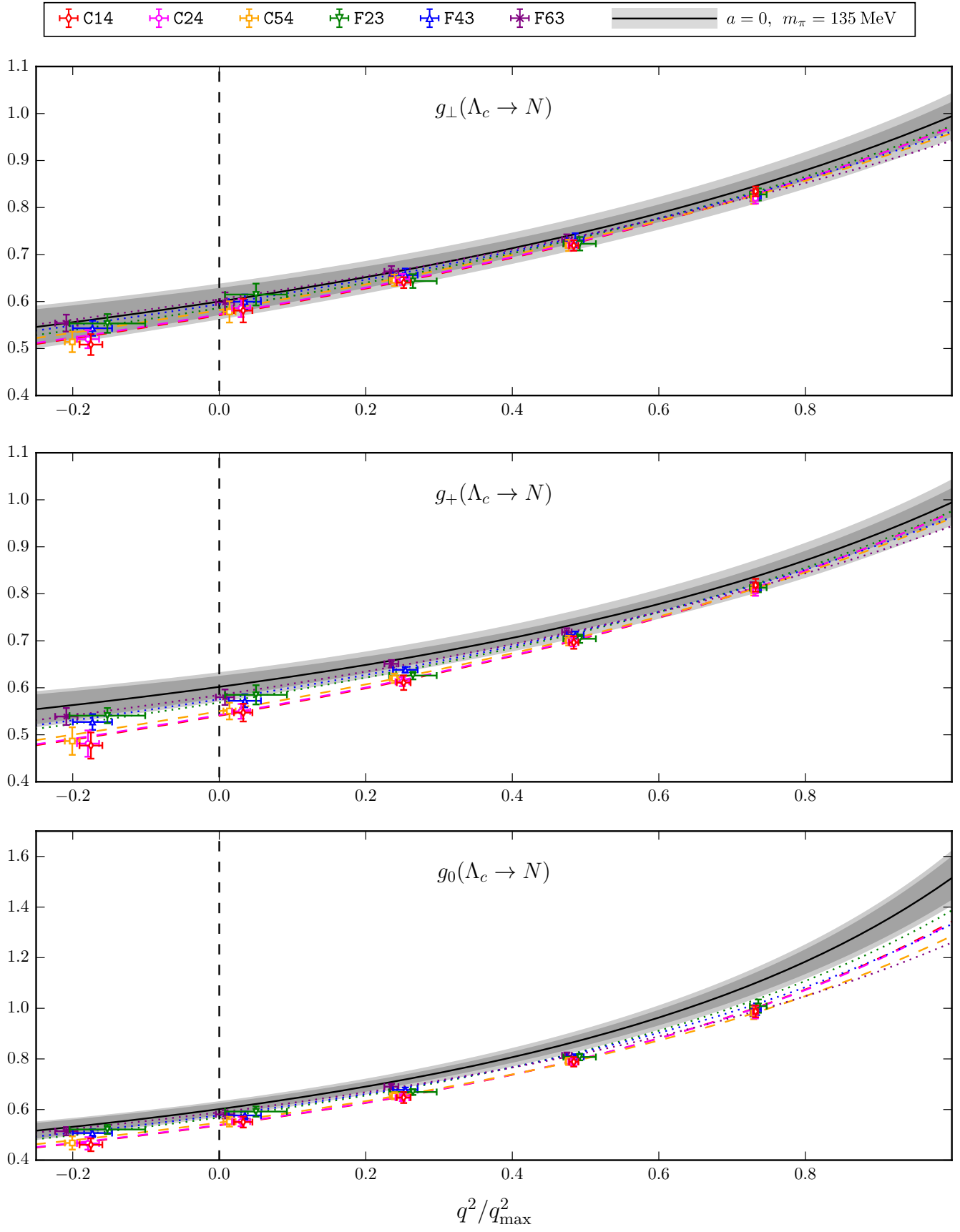


FIG. 3. Like Fig. 2, for the axial vector form factors.

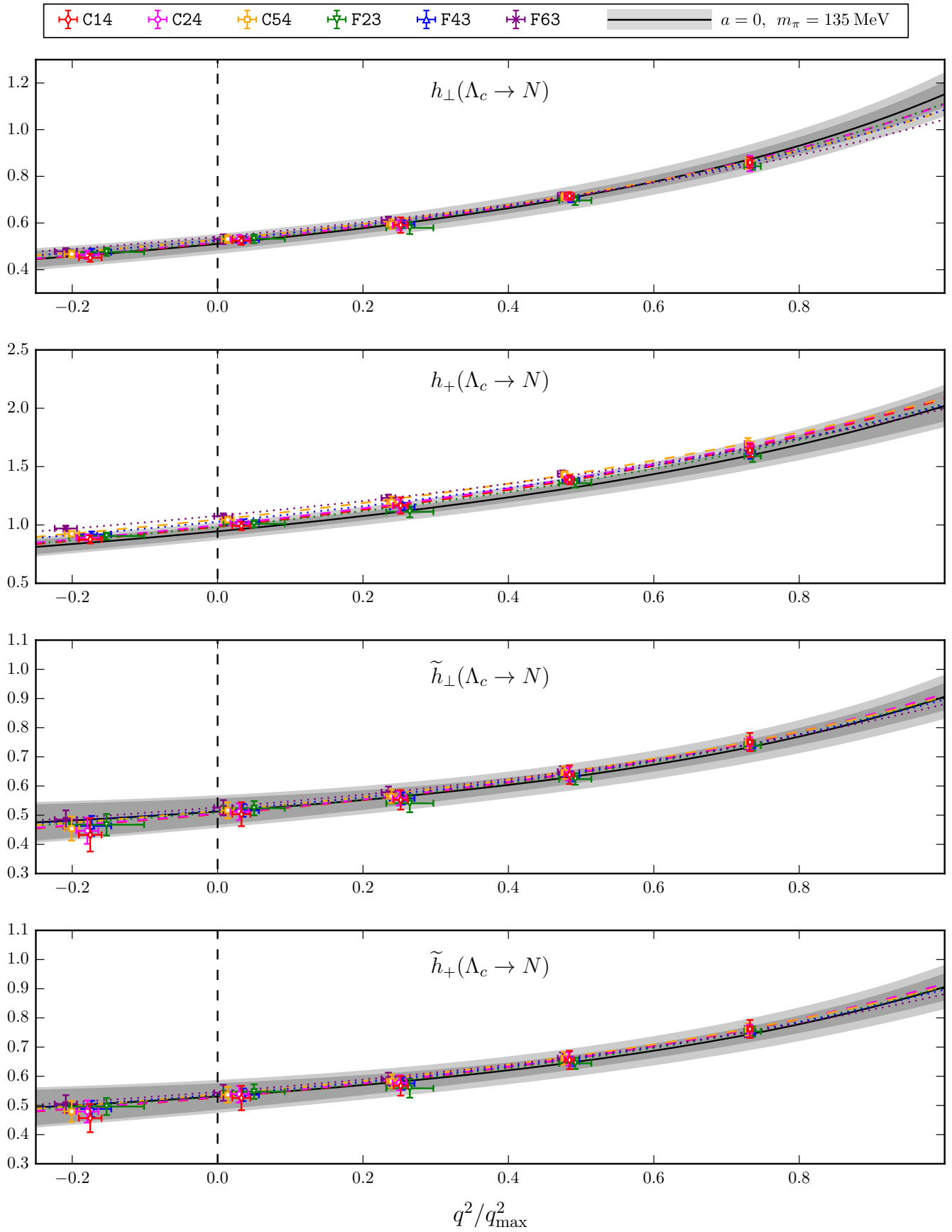


FIG. 4. Like Fig. 2, for the tensor form factors.

	Nominal fit	Higher-order fit
$a_0^{f\perp}$	1.36 ± 0.07	1.32 ± 0.09
$a_1^{f\perp}$	-1.70 ± 0.83	-1.33 ± 0.98
$a_2^{f\perp}$	0.71 ± 4.34	-1.38 ± 8.60
$a_3^{f\perp}$		7.02 ± 29.2
a_0^{f+}	0.83 ± 0.04	0.80 ± 0.05
a_1^{f+}	-2.33 ± 0.56	-1.94 ± 0.83
a_2^{f+}	8.41 ± 3.05	5.33 ± 8.04
a_3^{f+}		10.1 ± 28.8
a_0^{f0}	0.84 ± 0.04	0.82 ± 0.05
a_1^{f0}	-2.57 ± 0.60	-2.42 ± 0.88
a_2^{f0}	9.87 ± 3.15	7.71 ± 8.19
a_3^{f0}		9.30 ± 28.8
$a_0^{g\perp, g+}$	0.69 ± 0.02	0.68 ± 0.03
$a_1^{g\perp}$	-0.68 ± 0.32	-0.89 ± 0.58
$a_2^{g\perp}$	0.70 ± 2.18	3.97 ± 6.81
$a_3^{g\perp}$		-10.8 ± 25.2
a_1^{g+}	-0.90 ± 0.29	-1.07 ± 0.55
a_2^{g+}	2.25 ± 1.90	3.46 ± 6.42
a_3^{g+}		0.49 ± 24.1
a_0^{g0}	0.73 ± 0.04	0.71 ± 0.05
a_1^{g0}	-0.97 ± 0.52	-0.93 ± 0.77
a_2^{g0}	0.83 ± 2.61	1.64 ± 7.87
a_3^{g0}		-1.73 ± 28.0
$a_0^{h\perp}$	0.63 ± 0.03	0.62 ± 0.05
$a_1^{h\perp}$	-1.04 ± 0.45	-0.88 ± 0.72
$a_2^{h\perp}$	1.42 ± 2.67	1.42 ± 7.74
$a_3^{h\perp}$		-0.41 ± 27.8
a_0^{h+}	1.11 ± 0.07	1.10 ± 0.10
a_1^{h+}	-0.69 ± 0.92	-0.56 ± 1.07
a_2^{h+}	-2.84 ± 5.19	-3.85 ± 9.28
a_3^{h+}		5.61 ± 29.5
$a_0^{\tilde{h}\perp, \tilde{h}+}$	0.63 ± 0.03	0.63 ± 0.05
$a_1^{\tilde{h}\perp}$	-1.39 ± 0.58	-1.55 ± 0.81
$a_2^{\tilde{h}\perp}$	4.22 ± 3.97	6.20 ± 8.12
$a_3^{\tilde{h}\perp}$		-5.19 ± 28.3
$a_1^{\tilde{h}+}$	-1.19 ± 0.56	-1.23 ± 0.80
$a_2^{\tilde{h}+}$	3.73 ± 3.73	4.36 ± 8.08
$a_3^{\tilde{h}+}$		-0.84 ± 28.1

TABLE V. Results for the z -expansion parameters describing the form factors in the physical limit via Eq. (10). As explained in the main text, the nominal fit is used to evaluate the central values and statistical uncertainties, while the higher-order fit is used to estimate systematic uncertainties. Because of the endpoint constraints (7) and (8) at $z = 0$, the parameters $a_0^{g\perp, g+}$ and $a_0^{\tilde{h}\perp, \tilde{h}+}$ are common to the form factors g_\perp, g_+ and $\tilde{h}_\perp, \tilde{h}_+$, respectively. Files containing the parameter values with more digits and the full covariance matrices are provided as supplemental material.

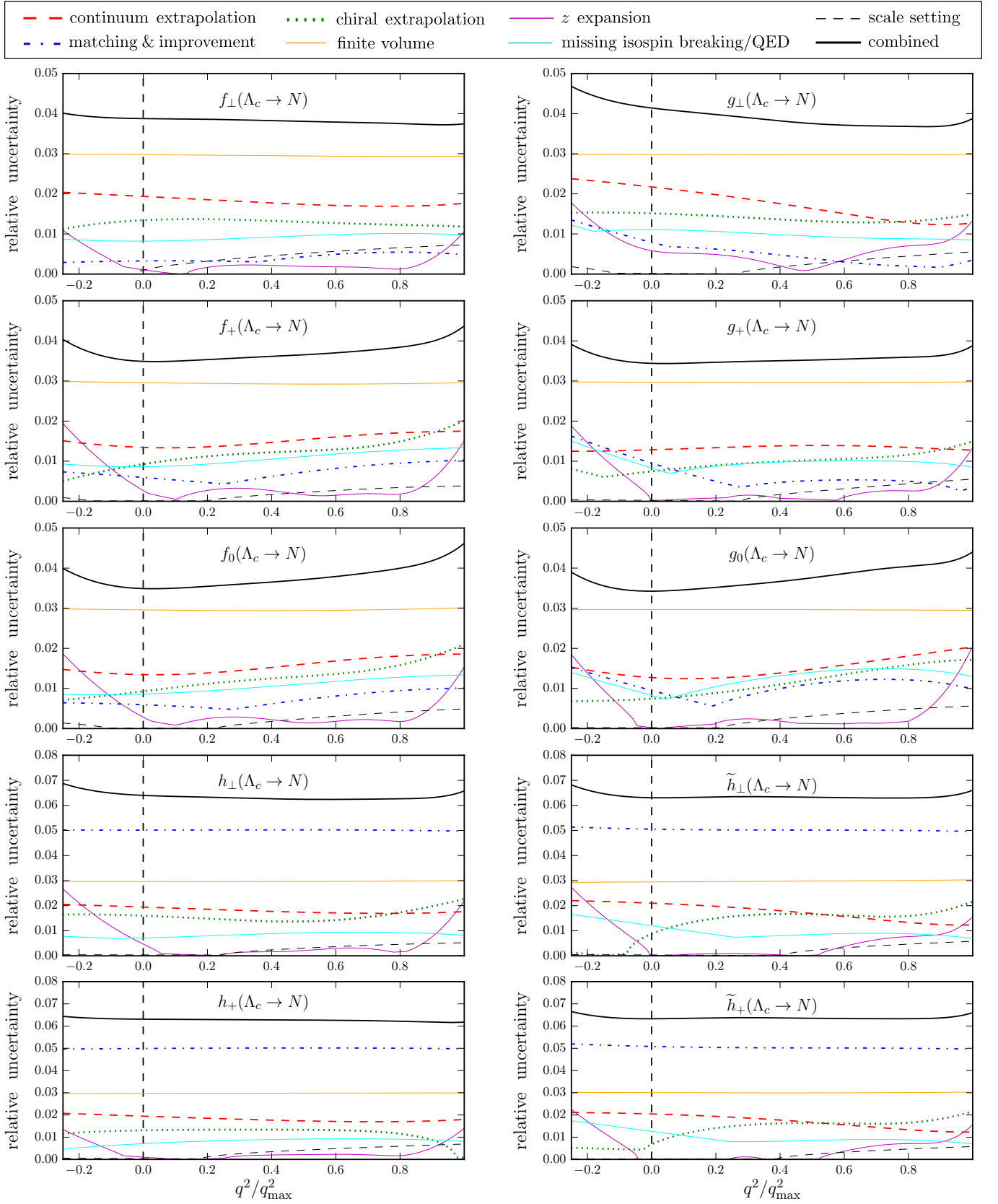


FIG. 5. Breakdown of systematic uncertainties in the form factors. The individual uncertainties are shown for illustration only; the combined systematic uncertainty is evaluated directly using the full higher-order fit.

IV. PHENOMENOLOGY OF $\Lambda_c \rightarrow n \ell^+ \nu_\ell$

In terms of the helicity form factors, the $\Lambda_c \rightarrow n \ell^+ \nu_\ell$ differential decay rate in the Standard Model reads

$$\begin{aligned} \frac{d\Gamma}{dq^2} = & \frac{G_F^2 |V_{cd}|^2 \sqrt{s_+ s_-}}{768 \pi^3 m_{\Lambda_c}^3} \left(1 - \frac{m_\ell^2}{q^2}\right)^2 \\ & \times \left\{ 4 (m_\ell^2 + 2q^2) \left(s_+ [g_\perp]^2 + s_- [f_\perp]^2 \right) \right. \\ & + 2 \frac{m_\ell^2 + 2q^2}{q^2} \left(s_+ [(m_{\Lambda_c} - m_N) g_+]^2 + s_- [(m_{\Lambda_c} + m_N) f_+]^2 \right) \\ & \left. + \frac{6m_\ell^2}{q^2} \left(s_+ [(m_{\Lambda_c} - m_N) f_0]^2 + s_- [(m_{\Lambda_c} + m_N) g_0]^2 \right) \right\}. \end{aligned} \quad (17)$$

Evaluating this expression for $\ell = e$ and $\ell = \mu$ using the form factor results described in the previous section gives the results shown in Fig. 6. The q^2 -integrated rates are

$$\frac{\Gamma(\Lambda_c \rightarrow n e^+ \nu_e)}{|V_{cd}|^2} = (0.405 \pm 0.016_{\text{stat}} \pm 0.020_{\text{syst}}) \text{ ps}^{-1}, \quad (18)$$

$$\frac{\Gamma(\Lambda_c \rightarrow n \mu^+ \nu_\mu)}{|V_{cd}|^2} = (0.396 \pm 0.016_{\text{stat}} \pm 0.020_{\text{syst}}) \text{ ps}^{-1}, \quad (19)$$

with statistical and systematic uncertainties from the form factors. Using $|V_{cd}| = 0.22497(67)$ from UTFit [36] and the Λ_c lifetime $\tau_{\Lambda_c} = 0.200(6)$ ps from the Particle Data Group [34] yields the branching fractions

$$\mathcal{B}(\Lambda_c \rightarrow n e^+ \nu_e) = (0.410 \pm 0.026_{\text{LQCD}} \pm 0.012_{\tau_{\Lambda_c}} \pm 0.002_{|V_{cd}|}) \%, \quad (20)$$

$$\mathcal{B}(\Lambda_c \rightarrow n \mu^+ \nu_\mu) = (0.400 \pm 0.026_{\text{LQCD}} \pm 0.012_{\tau_{\Lambda_c}} \pm 0.002_{|V_{cd}|}) \%, \quad (21)$$

where the uncertainties labeled ‘‘LQCD’’ are the total uncertainties resulting from the form factors.

Previous predictions for $\Gamma(\Lambda_c \rightarrow n e^+ \nu_e)/|V_{cd}|^2$ and $\Gamma(\Lambda_c \rightarrow n \mu^+ \nu_\mu)/|V_{cd}|^2$ are summarized in Table VI. All references included there predicted decay rates somewhat lower¹ than the lattice QCD results (18) and (19). While Refs. [1, 2, 5, 7] and [8] estimated the $\Lambda_c \rightarrow n$ form factors using quark models and light-cone sum rules, respectively, Ref. [6] derived $\mathcal{B}(\Lambda_c \rightarrow n e^+ \nu_e)$ from the BESIII experimental result for $\mathcal{B}(\Lambda_c \rightarrow \Lambda e^+ \nu_e)$ [37] using flavor $SU(3)$

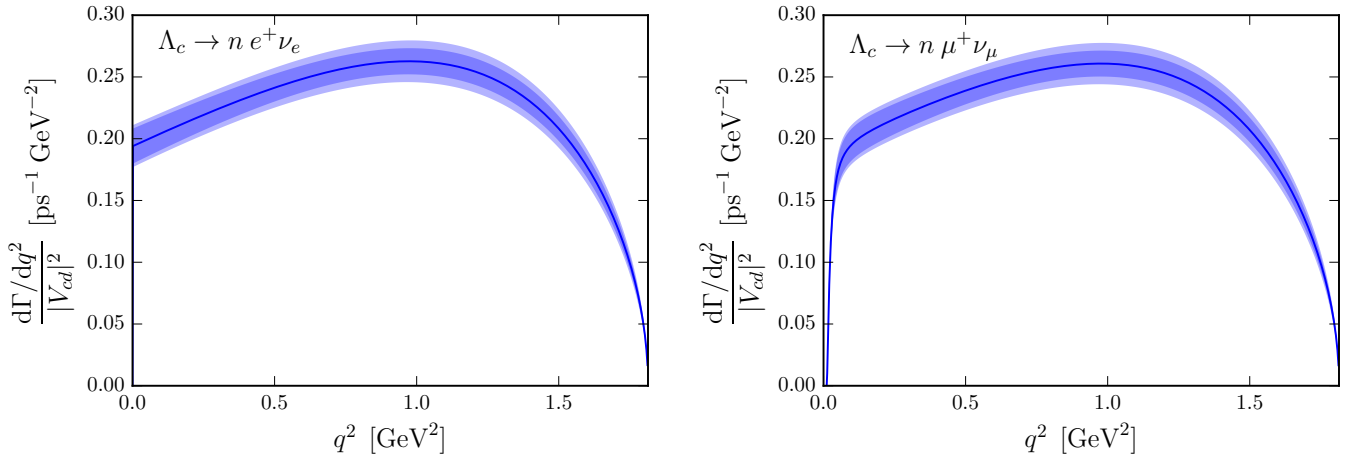


FIG. 6. Predictions for the $\Lambda_c \rightarrow n e^+ \nu_e$ and $\Lambda_c \rightarrow n \mu^+ \nu_\mu$ differential decay rates in the Standard Model, without the factor of $|V_{cd}|^2$. The inner and outer bands show the statistical and total uncertainty originating from the form factors.

¹ Reference [3] reported values for $\Gamma/|V_{cd}|^2$ that are higher than calculated here by an order of magnitude, but these values appear to be inconsistent with the form factor parameterizations given in the same work, and are therefore not included here.

Reference	Method	$\Gamma(\Lambda_c \rightarrow n e^+ \nu_e)/ V_{cd} ^2$ [ps ⁻¹]	$\Gamma(\Lambda_c \rightarrow n \mu^+ \nu_\mu)/ V_{cd} ^2$ [ps ⁻¹]
Ivanov <i>et al.</i> , 1996 [1]	Quark model	0.26	
Pervin <i>et al.</i> , 2005 [2]	Quark model	0.203, 0.269	
Gutsche <i>et al.</i> , 2014 [5]	Quark model	0.20	0.19
Lü <i>et al.</i> , 2016 [6]	$SU(3)$ symmetry	0.289 ± 0.035	
Faustov and Galkin, 2016 [7]	Quark model	0.265	0.260
Li <i>et al.</i> , 2016 [8]	Light-cone sum rules	0.267 ± 0.011	
This work	Lattice QCD	0.405 ± 0.026	0.396 ± 0.025

TABLE VI. Comparison of predictions for $\Gamma(\Lambda_c \rightarrow n e^+ \nu_e)/|V_{cd}|^2$ and $\Gamma(\Lambda_c \rightarrow n \mu^+ \nu_\mu)/|V_{cd}|^2$ with the lattice QCD results obtained here. The two different values from Ref. [2] correspond to nonrelativistic and semirelativistic kinetic terms in the model. Reference [6] predicted the branching fraction, which was converted here using $|V_{cd}| = 0.22497(67)$ [36] and $\tau_{\Lambda_c} = 0.200(6)$ ps [34]. Reference [8] gave a value for Γ , which was converted using the value of $|V_{cd}|$ given there.

Reference	Method	$f_1(0)$	$f_2(0)$	$g_1(0)$	$g_2(0)$
A. Khodjamirian <i>et al.</i> , 2011 [4]	LCSR, $\eta_{\Lambda_c}^{(A)}$	$0.46^{+0.15}_{-0.11}$	$-0.32^{+0.08}_{-0.07}$	$0.49^{+0.14}_{-0.11}$	$-0.20^{+0.09}_{-0.06}$
	LCSR, $\eta_{\Lambda_c}^{(P)}$	$0.59^{+0.15}_{-0.16}$	$-0.43^{+0.13}_{-0.12}$	$0.55^{+0.14}_{-0.15}$	$-0.16^{+0.08}_{-0.05}$
This work	Lattice QCD	0.672 ± 0.039	-0.321 ± 0.038	0.602 ± 0.031	0.003 ± 0.052

TABLE VII. Comparison of $\Lambda_c \rightarrow N$ form factor values at $q^2 = 0$ calculated in Ref. [4] using QCD light-cone sum rules for two different Λ_c interpolating fields, $\eta_{\Lambda_c}^{(A)}$ and $\eta_{\Lambda_c}^{(P)}$, with the present lattice QCD results. The form factors defined in Ref. [4] are related to the helicity form factors as $f_1 = [(m_{\Lambda_c} + m_N)^2 f_+ - q^2 f_\perp]/s_+$, $f_2 = m_{\Lambda_c}(m_{\Lambda_c} + m_N)(f_+ - f_\perp)/s_+$, $g_1 = [(m_{\Lambda_c} - m_N)^2 g_+ - q^2 g_\perp]/s_-$, and $g_2 = m_{\Lambda_c}(m_{\Lambda_c} - m_N)(g_+ - g_\perp)/s_-$.

symmetry. The low rate obtained in that way can likely be attributed in part to the assumption $m_n = m_\Lambda$, which results in an underestimated phase space.

The authors of Ref. [4] also calculated the $\Lambda_c \rightarrow N$ form factors using QCD light-cone sum rules, but only at $q^2 = 0$. As shown in Table VII, the results are consistent with the lattice QCD determination within 1 to 2 σ .

V. PHENOMENOLOGY OF $\Lambda_c \rightarrow p \mu^+ \mu^-$

The theory of exclusive $c \rightarrow u \ell^+ \ell^-$ transitions in the Standard Model is complicated by the dominance of nonlocal hadronic matrix elements that cannot easily be calculated in lattice QCD. The form factors computed in this work only describe local matrix elements of the form $\langle p | \bar{u} \Gamma c | \Lambda_c \rangle$. In the following, two different approaches for expressing the $\Lambda_c \rightarrow p \mu^+ \mu^-$ observables in terms of these form factors will be considered: a perturbative calculation of effective Wilson coefficients at next-to-next-to-leading order (Sec. VA), and a phenomenological Breit-Wigner model for the contributions of intermediate ϕ , ω , and ρ^0 resonances (Sec. VB). The resulting predictions for the $\Lambda_c \rightarrow p \mu^+ \mu^-$ differential branching fraction and angular distribution are given in Sec. VC. In the effective-field-theory description, possible heavy new physics beyond the Standard Model contributes only via the local matrix elements given by the form factors. In the case of $\Lambda_c \rightarrow p \mu^+ \mu^-$ (but not, for example, in lepton-flavor-violating modes such as $\Lambda_c \rightarrow p e^+ \mu^-$), such contributions still interfere with Standard-Model contributions. Nevertheless, the $\Lambda_c \rightarrow p \mu^+ \mu^-$ forward-backward asymmetry is nonzero only in the presence of new physics, and therefore provides a clean test of the Standard Model.

A. Standard-Model Wilson coefficients in perturbation theory

The $c \rightarrow u \ell^+ \ell^-$ effective weak Lagrangian at $\mu < m_b$, after integrating out the b quark, has the form

$$\mathcal{L}_{\text{eff}} = \frac{4G_F}{\sqrt{2}} \sum_{q=d,s} V_{cq}^* V_{uq} \left(\tilde{C}_1 P_1^{(q)} + \tilde{C}_2 P_2^{(q)} + \sum_{i=3}^{10} \tilde{C}_i P_i \right), \quad (22)$$

where $P_{1,\dots,6}$ are four-quark operators, P_7 and P_8 are electromagnetic and gluonic dipole operators, and P_9, P_{10} are semileptonic operators [9, 38]. Following Refs. [9, 39], the matrix elements are written as

$$\langle \mathcal{L}_{\text{eff}} \rangle = \frac{4G_F \alpha_e}{\sqrt{2}} \frac{1}{4\pi} \sum_i C_i(q^2) \langle Q_i \rangle, \quad (23)$$

with rescaled electromagnetic dipole and semileptonic operators

$$Q_7 = \frac{m_c}{e} (\bar{u} \sigma^{\mu\nu} P_{Rc}) F_{\mu\nu}, \quad (24)$$

$$Q_9 = (\bar{u} \gamma_\mu P_{Lc}) (\bar{\ell} \gamma^\mu \ell), \quad (25)$$

$$Q_{10} = (\bar{u} \gamma_\mu P_{Lc}) (\bar{\ell} \gamma^\mu \gamma_5 \ell), \quad (26)$$

and q^2 -dependent effective Wilson coefficients

$$C_{7,9}(q^2) = \frac{4\pi}{\alpha_s} \left[V_{cd}^* V_{ud} C_{7,9}^{\text{eff}(d)}(q^2) + V_{cs}^* V_{us} C_{7,9}^{\text{eff}(s)}(q^2) \right], \quad (27)$$

which include the perturbative matrix elements of the four-quark and gluonic dipole operators. The Wilson coefficient C_{10} is zero in the Standard Model due to CKM unitarity, since all down-type quarks are treated as massless at $\mu = m_W$ and C_{10} does not mix under renormalization [38, 39]. At next-to-next-to-leading order, including the recently derived two-loop QCD matrix elements of $P_1^{(q)}$ and $P_2^{(q)}$ for arbitrary momentum transfer [39, 40], the effective Wilson coefficients are given by

$$\begin{aligned} C_9^{\text{eff}(q)}(q^2) &= \tilde{C}_9^{(0+1+2)} + \frac{\alpha_s}{4\pi} \left[\frac{8}{27} \tilde{C}_1 + \frac{2}{9} \tilde{C}_2 - \frac{8}{9} \tilde{C}_3 - \frac{32}{27} \tilde{C}_4 - \frac{128}{9} \tilde{C}_5 - \frac{512}{27} \tilde{C}_6 \right. \\ &\quad + L(m_c^2, q^2) \left(\frac{28}{9} \tilde{C}_3 + \frac{16}{27} \tilde{C}_4 + \frac{304}{9} \tilde{C}_5 + \frac{256}{27} \tilde{C}_6 \right) \\ &\quad + L(m_s^2, q^2) \left(-\frac{4}{3} \tilde{C}_3 - \frac{40}{3} \tilde{C}_5 \right) \\ &\quad + L(0, q^2) \left(\frac{16}{9} \tilde{C}_3 + \frac{16}{27} \tilde{C}_4 + \frac{184}{9} \tilde{C}_5 + \frac{256}{27} \tilde{C}_6 \right) \\ &\quad \left. + (\delta_{qs} L(m_s^2, q^2) + \delta_{qd} L(0, q^2)) \left(-\frac{8}{27} \tilde{C}_1 - \frac{2}{9} \tilde{C}_2 \right) \right]^{(0+1)} \\ &\quad + \left(\frac{\alpha_s}{4\pi} \right)^2 \left[F_{1,q}^{(9)}(m_c^2, q^2) \tilde{C}_1^{(0)} + F_{2,q}^{(9)}(m_c^2, q^2) \tilde{C}_2^{(0)} + F_8^{(9)}(m_c^2, q^2) C_8^{\text{eff}} \right] \end{aligned} \quad (28)$$

and

$$\begin{aligned} C_7^{\text{eff}(q)}(q^2) &= \tilde{C}_7^{(0+1+2)} + \frac{\alpha_s}{4\pi} \left[\frac{2}{3} \tilde{C}_3 + \frac{8}{9} \tilde{C}_4 + \frac{40}{3} \tilde{C}_5 + \frac{160}{9} \tilde{C}_6 \right]^{(0+1)} \\ &\quad + \left(\frac{\alpha_s}{4\pi} \right)^2 \left[\left(-\frac{1}{6} \tilde{C}_1^{(0)} + \tilde{C}_2^{(0)} \right) F_{2,q}^{(7)}(m_c^2, q^2) + F_8^{(7)}(m_c^2, q^2) C_8^{\text{eff}} \right], \end{aligned} \quad (29)$$

where the Wilson coefficients \tilde{C}_i are expanded in the strong coupling as

$$\tilde{C}_i = \tilde{C}_i^{(0)} + \frac{\alpha_s}{4\pi} \tilde{C}_i^{(1)} + \left(\frac{\alpha_s}{4\pi} \right)^2 \tilde{C}_i^{(2)} + \dots, \quad (30)$$

and the notation $\tilde{C}_i^{(0+1)} \equiv \tilde{C}_i^{(0)} + \frac{\alpha_s}{4\pi} \tilde{C}_i^{(1)}$ etc. is used. Above,

$$C_8^{\text{eff}} = \tilde{C}_8^{(1)} + \tilde{C}_3^{(0)} - \frac{1}{6} \tilde{C}_4^{(0)} + 20 \tilde{C}_5^{(0)} - \frac{10}{3} \tilde{C}_6^{(0)}. \quad (31)$$

The functions $L(m^2, q^2)$, $L(0, q^2)$, $F_8^{(7)}(m_c^2, q^2)$, and $F_8^{(9)}(m_c^2, q^2)$ can be found in Appendix B of Ref. [9]. The functions $F_{1,q}^{(9)}(m_c^2, q^2)$, $F_{2,q}^{(9)}(m_c^2, q^2)$, and $F_{1,q}^{(7)}(m_c^2, q^2) = -\frac{1}{6} F_{2,q}^{(7)}(m_c^2, q^2)$ are given in Ref. [40], and were evaluated here using

the files `fit_F*.dat` provided as supplemental material in Ref. [40]. The values of $\tilde{C}_i^{(0)}$, $\frac{\alpha_s}{4\pi}\tilde{C}_i^{(1)}$, and $(\frac{\alpha_s}{4\pi})^2\tilde{C}_i^{(2)}$ at $\mu = m_c$ were taken from Table 2.2 of Ref. [39]. For the purpose of estimating the perturbative uncertainties in the observables, the values of these coefficients were provided by Stefan de Boer additionally for $\mu = \sqrt{2}m_c$ and $\mu = m_c/\sqrt{2}$ [41]. The low-energy value of α_e was used, and the strong coupling $\alpha_s(\mu)$ for four flavors was evaluated using the `RunDec` package [42]. The quark masses were set to $m_c^{\overline{\text{MS}}} = 1.27$ GeV, $m_c^{\text{pole}} = 1.47$ GeV, $m_s^{\text{pole}} = 0.13$ GeV as in Ref. [40]. The CKM matrix elements were taken from UTFit [36].

B. Breit-Wigner model of resonant contributions

Similarly to Ref. [9], the contributions from intermediate ϕ , ω , and ρ^0 resonances were modeled using an effective Wilson coefficient $C_9^{\text{R}}(q^2)$ given by

$$C_9^{\text{R}}(q^2) = a_\omega e^{i\delta_\omega} \left(\frac{1}{q^2 - m_\omega^2 + im_\omega\Gamma_\omega} - \frac{3}{q^2 - m_\rho^2 + im_\rho\Gamma_\rho} \right) + \frac{a_\phi e^{i\delta_\phi}}{q^2 - m_\phi^2 + im_\phi\Gamma_\phi}, \quad (32)$$

and setting $C_7(q^2) = 0$. Here, the relative magnitude and sign between the ρ^0 and ω amplitudes were fixed as for $D^+ \rightarrow \pi^+\ell^+\ell^-$ in Ref. [43]. In the case of $\Lambda_c \rightarrow p\ell^+\ell^-$, the quark flow diagrams are different, but those diagrams that are expected to dominate yield the same relation. The resonance masses and widths were taken from the Particle Data Group [34]. To determine the couplings a_ω and a_ϕ , the $\Lambda_c \rightarrow p\mu^+\mu^-$ branching fraction was computed using only $C_9^{\text{R}}(q^2)$ and keeping only the ω or ϕ contribution, and demanding that

$$\mathcal{B}(\Lambda_c(\rightarrow pV) \rightarrow p\mu^+\mu^-) = \mathcal{B}(\Lambda_c \rightarrow pV) \mathcal{B}(V \rightarrow \mu^+\mu^-) \quad \text{for } V = \omega, \phi, \quad (33)$$

where the right-hand side was evaluated using the following experimental inputs:

$$\mathcal{B}(\Lambda_c \rightarrow p\phi) = (1.08 \pm 0.14) \times 10^{-3} \quad [34], \quad (34)$$

$$\mathcal{B}(\phi \rightarrow \mu^+\mu^-) = (2.87 \pm 0.19) \times 10^{-4} \quad [34], \quad (35)$$

$$\frac{\mathcal{B}(\Lambda_c \rightarrow p\omega)\mathcal{B}(\omega \rightarrow \mu^+\mu^-)}{\mathcal{B}(\Lambda_c \rightarrow p\phi)\mathcal{B}(\phi \rightarrow \mu^+\mu^-)} = 0.23 \pm 0.08 \pm 0.03 \quad [12]. \quad (36)$$

This procedure gives

$$a_\omega = 0.068 \pm 0.013, \quad (37)$$

$$a_\phi = 0.111 \pm 0.008. \quad (38)$$

The phases δ_ω and δ_ϕ were varied independently in the ranges 0 to 2π when calculating the $\Lambda_c \rightarrow p\mu^+\mu^-$ observables presented in the next section.

C. Results for the $\Lambda_c \rightarrow p\mu^+\mu^-$ observables

The two-fold differential decay rate of $\Lambda_c \rightarrow p\ell^+\ell^-$ with unpolarized Λ_c can be written as

$$\frac{d^2\Gamma}{dq^2 d\cos\theta_\ell} = \frac{3}{2} (K_{1ss} \sin^2\theta_\ell + K_{1cc} \cos^2\theta_\ell + K_{1c} \cos\theta_\ell), \quad (39)$$

where θ_ℓ is the angle of the ℓ^+ in the dilepton rest frame with respect to the direction of flight of the dilepton system in the Λ_c rest frame, and the coefficients K_{1ss} , K_{1cc} , and K_{1c} are functions of q^2 . The q^2 -differential decay rate is obtained by integrating over $\cos\theta_\ell$,

$$\frac{d\Gamma}{dq^2} = 2K_{1ss} + K_{1cc}. \quad (40)$$

The fraction of longitudinally polarized dimuons and the forward-backward asymmetry are defined as

$$F_L = \frac{2K_{1ss} - K_{1cc}}{d\Gamma/dq^2} \quad (41)$$

and

$$A_{FB} = \frac{3}{2} \frac{K_{1c}}{d\Gamma/dq^2}. \quad (42)$$

For the effective Lagrangian (23) with operators Q_7, Q_9, Q_{10} , the expressions for K_{1ss}, K_{1cc} , and K_{1c} in terms of the form factors and the Wilson coefficients $C_i(q^2)$ can be obtained from Ref. [44] (in the approximation $m_\ell = 0$) or Ref. [45] (for $m_\ell \neq 0$; used here). These references consider the similar process $\Lambda_b \rightarrow \Lambda \ell^+ \ell^-$; to adapt the equations to $\Lambda_c \rightarrow p \ell^+ \ell^-$, the factor of $|V_{tb} V_{ts}^*|^2$ needs to be removed and the masses need to be replaced appropriately.

The predictions for $d\mathcal{B}/dq^2 = \tau_{\Lambda_c} d\Gamma/dq^2$, F_L , and A_{FB} for $\Lambda_c \rightarrow p \mu^+ \mu^-$, using either the perturbative Wilson coefficients (28) and (29) or the resonant model (32), are shown in the left panels of Fig. 7. In the right panels, an example new-physics contribution of $C_9^{\text{NP}} = -0.6$, $C_{10}^{\text{NP}} = 0.6$ was added to the Wilson coefficients to illustrate the effect on the observables. A contribution of this magnitude is not yet excluded by experimental measurements of rare charm meson decays [9]. Also shown in Fig. 7 is the LHCb upper limit of $\mathcal{B}(\Lambda_c \rightarrow p \mu^+ \mu^-) < 7.7 \times 10^{-8}$ (at 90% confidence level) in the $\sqrt{q^2}$ region excluding ± 40 MeV intervals around m_ω and m_ϕ [12]. The LHCb upper limit on $\mathcal{B}(\Lambda_c \rightarrow p \mu^+ \mu^-)$ also does not yet exclude the new-physics scenario considered here, but comes close.

The error bands of the nonresonant SM predictions are dominated by the perturbative uncertainty, which was estimated by computing the changes in the observables when varying the renormalization scale from $\mu = m_c$ to $\mu = \sqrt{2} m_c$ and $\mu = m_c/\sqrt{2}$. While doing this scale variation, the renormalization-group running of the tensor form factors was included for consistency, by multiplying these form factors with

$$\left(\frac{\alpha_s(\mu)}{\alpha_s(m_c)} \right)^{-\gamma_T^{(0)}/(2\beta_0)}, \quad (43)$$

where $\gamma_T^{(0)} = 2C_F = 8/3$ is the anomalous dimension of the tensor current [46] and $\beta_0 = (11N_c - 2N_f)/3 = 25/3$ is the leading-order coefficient of the QCD beta function for 4 active flavors. The error bands of the predictions using the resonant model (32) are dominated by the phase uncertainty, which was estimated by independently varying δ_ω and δ_ϕ in the ranges 0 to 2π and showing the resulting ranges of the observables, and the uncertainties in the couplings a_ω and a_ϕ as given in Eqs. (37) and (38).

The branching fractions integrated over the entire q^2 range are found to be

$$\mathcal{B}(\Lambda_c \rightarrow p \mu^+ \mu^-)_{\text{Perturbative SM}} = (4.1 \pm 0.4_{-1.9}^{+6.1}) \times 10^{-11}, \quad (44)$$

$$\mathcal{B}(\Lambda_c \rightarrow p \mu^+ \mu^-)_{\text{Resonances}} = (3.7_{-1.2}^{+1.1}) \times 10^{-7}, \quad (45)$$

where, for the perturbative SM prediction, the first uncertainty given is the form factor uncertainty from the lattice calculation, and the second uncertainty is the perturbative uncertainty estimated by varying the renormalization scale. As can be seen in Fig. 7, the low- q^2 region gives most of the perturbative SM contribution.

The value for $\mathcal{B}(\Lambda_c \rightarrow p \mu^+ \mu^-)_{\text{Perturbative SM}}$ calculated here is approximately 10^3 times higher than that obtained in Refs. [47, 48]. While [47] does not give a reference for the Wilson coefficients, [48] reportedly uses Wilson coefficients from Ref. [49]. The Wilson coefficients from Ref. [49] actually tend to give higher branching ratios than the Wilson coefficients employed here [38–41], and the very small branching fractions obtained in [47, 48] are puzzling. Note that Refs. [47, 48] write the matrix elements of the tensor current in terms of six form factors, of which only four are independent. The numerical parameterizations given there for the six tensor form factors violate the exact kinematical relations between these form factors.

The $\Lambda_c \rightarrow p \mu^+ \mu^-$ forward-backward asymmetry, shown at the bottom of Fig. 7, vanishes in the Standard Model because it contains an overall factor of C_{10} . New physics giving a nonzero C_{10} would produce a nonzero forward-backward asymmetry, as shown in the bottom-right panel of Fig. 7. While the actual values of A_{FB} strongly depend on the details of the resonant contributions to C_9 , this observable still provides a clean null test of the Standard Model.

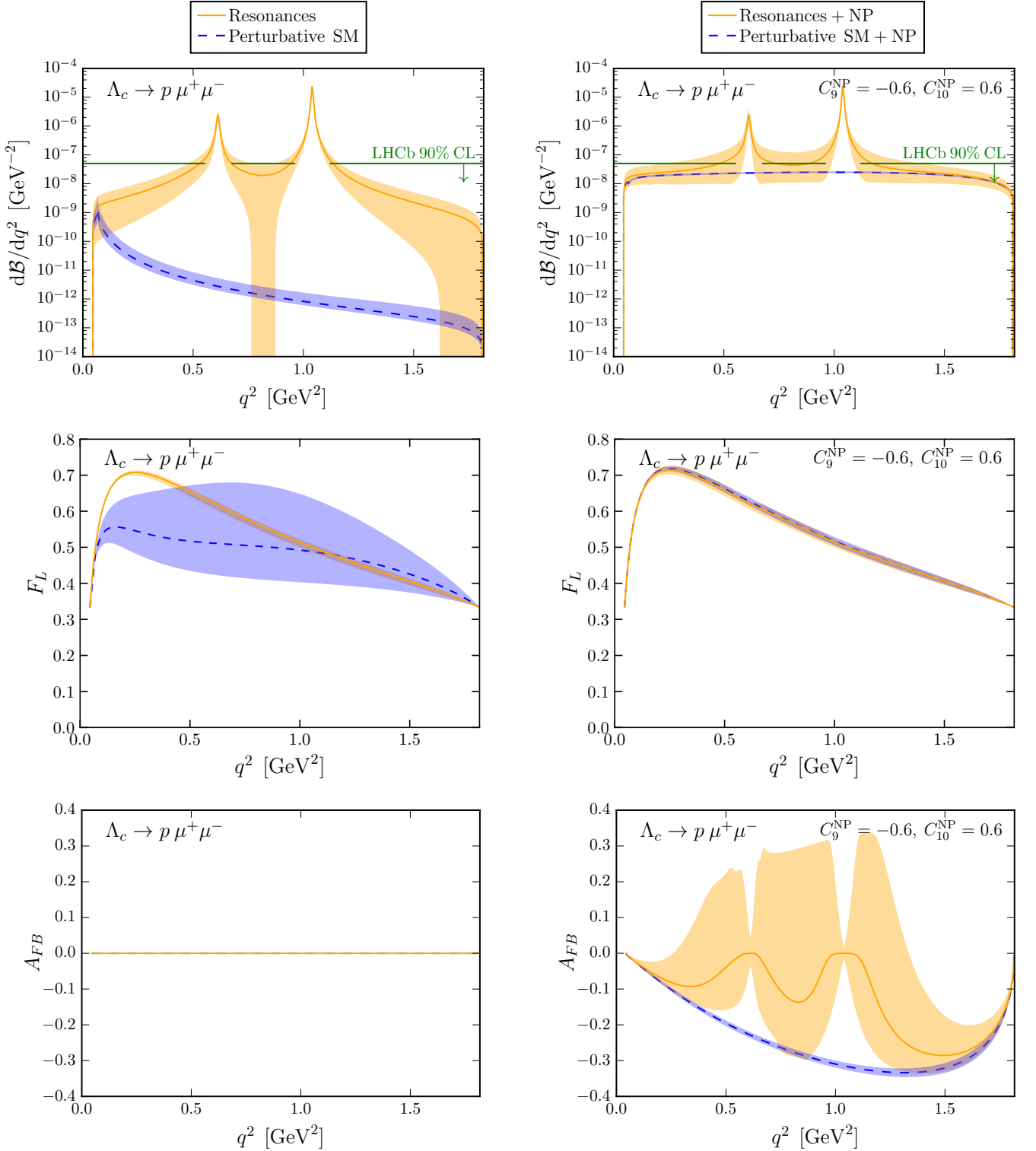


FIG. 7. Predictions for the $\Lambda_c \rightarrow p \mu^+ \mu^-$ differential branching fraction, fraction of longitudinally polarized dimuons, and forward-backward asymmetry, in the Standard Model (left panels) and with a new-physics contribution of $C_9^{\text{NP}} = -0.6$, $C_{10}^{\text{NP}} = 0.6$ (right panels). Also indicated is the LHCb upper limit (at 90% confidence level) on $\mathcal{B}(\Lambda_c \rightarrow p \mu^+ \mu^-)$ in the $\sqrt{q^2}$ region excluding ± 40 MeV intervals around m_ω and m_ϕ [12]. The blue dashed curves use the perturbative results (28) and (29) for the Standard-Model contribution, with error bands including the perturbative scale uncertainties and the form factor uncertainties. The orange solid curves instead use the resonant Breit-Wigner model (32) for the Standard-Model contribution, with error bands including the changes in the observables under independent variations of the phases δ_ω and δ_ϕ in the ranges 0 to 2π , as well as the uncertainties in the couplings a_ω and a_ϕ and the form factor uncertainties. The curves show the averages over all values of phases.

VI. CONCLUSIONS

In this paper, a precise lattice QCD determination of the $\Lambda_c \rightarrow N$ ($N = n, p$) vector, axial vector, and tensor form factors was reported. The results provide Standard-Model predictions for the $\Lambda_c \rightarrow n e^+ \nu_e$ and $\Lambda_c \rightarrow n \mu^+ \nu_\mu$ decay rates with an uncertainty of 6.4%. The rates calculated here for these decays are higher than those predicted in Refs. [1, 2, 5–8] using quark models, sum rules, or $SU(3)$ symmetry, by factors ranging from 1.4 to 2.

The form factors were then applied to study the differential branching fraction and angular distribution of the rare charm decay $\Lambda_c \rightarrow p \mu^+ \mu^-$, using either perturbative results for the effective Wilson coefficients in the Standard Model [38–40] or a simple Breit-Wigner model for the long-distance contributions from the ϕ , ω , and ρ^0 resonances. The perturbative analysis gives $\mathcal{B}(\Lambda_c \rightarrow p \mu^+ \mu^-)_{\text{Perturbative SM}} = (4.1 \pm 0.4_{-1.9}^{+6.1}) \times 10^{-11}$. The LHCb upper limit of $\mathcal{B}(\Lambda_c \rightarrow p \mu^+ \mu^-) < 7.7 \times 10^{-8}$ (at 90% confidence level) in the dimuon mass region excluding ± 40 MeV intervals around m_ω and m_ϕ [12] still allows new-physics contributions to C_9 and C_{10} [defined as in Eq. (23)] of order $\mathcal{O}(1)$.

The $\Lambda_c \rightarrow p \mu^+ \mu^-$ observables in the Standard Model are dominated by long-distance contributions from nonlocal matrix elements, whose treatment is still very unsatisfactory. However, the forward-backward asymmetry is nonzero only in the presence of new physics, and a measurement would provide a clean test of the Standard Model. More detailed phenomenological studies, including other observables such as CP asymmetries and lepton-flavor-violating decay modes, are warranted.

ACKNOWLEDGMENTS

I thank Stefan de Boer for providing the values of the $c \rightarrow u \ell^+ \ell^-$ Wilson coefficients for additional choices of the renormalization scale, and Christoph Lehner for computing the perturbative lattice-to-continuum matching and $\mathcal{O}(a)$ -improvement coefficients for the $c \rightarrow u$ currents. I am grateful to the RBC and UKQCD Collaborations for making their gauge field ensembles available. This work was supported by National Science Foundation Grant No. PHY-1520996 and by the RHIC Physics Fellow Program of the RIKEN BNL Research Center. High-performance computing resources were provided by the Extreme Science and Engineering Discovery Environment (XSEDE), supported by National Science Foundation Grant No. ACI-1053575, as well as the National Energy Research Scientific Computing Center, a DOE Office of Science User Facility supported by the Office of Science of the U.S. Department of Energy under Contract No. DE-AC02-05CH11231. The Chroma software system [50] was used for the lattice calculations.

NOTE ADDED

In this version, I corrected an error in the lepton-mass contributions to F_L in Fig. 7. I thank Gudrun Hiller for bringing this to my attention.

APPENDIX: LATTICE FORM FACTOR DATA

	$ \mathbf{p}' ^2/(2\pi/L)^2$	C14	C24	C54	F23	F43	F63
f_{\perp}	1	1.884(54)	1.897(35)	1.941(29)	1.869(43)	1.895(32)	1.947(33)
	2	1.567(44)	1.587(31)	1.629(28)	1.574(37)	1.599(30)	1.655(28)
	3	1.287(60)	1.300(47)	1.348(41)	1.290(49)	1.329(46)	1.396(40)
	4	1.122(41)	1.153(21)	1.190(21)	1.171(28)	1.185(23)	1.223(26)
	5	0.998(38)	1.025(27)	1.061(28)	1.055(23)	1.073(20)	1.113(21)
f_{+}	1	1.093(22)	1.085(16)	1.087(14)	1.070(13)	1.074(12)	1.087(15)
	2	0.883(22)	0.887(17)	0.894(15)	0.875(18)	0.884(15)	0.902(18)
	3	0.720(24)	0.725(20)	0.739(17)	0.706(22)	0.726(18)	0.752(20)
	4	0.638(25)	0.652(20)	0.658(17)	0.675(20)	0.667(18)	0.666(21)
	5	0.580(41)	0.601(47)	0.605(48)	0.613(28)	0.613(32)	0.620(24)
f_0	1	0.983(20)	0.969(17)	0.971(15)	0.967(16)	0.966(14)	0.970(17)
	2	0.822(20)	0.828(17)	0.833(15)	0.812(18)	0.824(16)	0.839(19)
	3	0.694(22)	0.701(19)	0.714(17)	0.680(22)	0.701(19)	0.726(19)
	4	0.635(23)	0.650(19)	0.657(17)	0.670(20)	0.664(18)	0.665(21)
	5	0.590(37)	0.610(42)	0.616(42)	0.625(26)	0.625(29)	0.636(18)
g_{\perp}	1	0.834(10)	0.820(11)	0.820(12)	0.828(13)	0.8246(93)	0.825(11)
	2	0.719(11)	0.720(11)	0.719(12)	0.723(14)	0.730(15)	0.732(11)
	3	0.640(12)	0.647(12)	0.645(12)	0.644(15)	0.656(14)	0.664(11)
	4	0.581(25)	0.586(19)	0.578(23)	0.615(23)	0.600(15)	0.598(21)
	5	0.508(22)	0.520(19)	0.514(22)	0.553(20)	0.543(16)	0.554(18)
g_{+}	1	0.818(14)	0.806(10)	0.807(11)	0.8130(96)	0.8121(76)	0.8149(97)
	2	0.696(13)	0.6977(97)	0.700(10)	0.7043(87)	0.7123(74)	0.7185(83)
	3	0.611(15)	0.6128(95)	0.620(10)	0.6260(82)	0.6383(61)	0.6510(81)
	4	0.547(19)	0.550(16)	0.550(18)	0.585(20)	0.572(14)	0.580(16)
	5	0.477(28)	0.481(28)	0.487(29)	0.541(16)	0.527(17)	0.539(18)
g_0	1	0.988(23)	0.985(24)	0.982(25)	1.009(26)	0.996(23)	0.990(22)
	2	0.789(19)	0.788(14)	0.790(14)	0.808(13)	0.808(10)	0.814(12)
	3	0.647(22)	0.647(13)	0.655(14)	0.669(11)	0.6775(93)	0.690(12)
	4	0.550(22)	0.553(18)	0.552(19)	0.592(20)	0.577(16)	0.581(16)
	5	0.461(25)	0.466(25)	0.468(26)	0.521(18)	0.507(15)	0.514(16)
h_{\perp}	1	0.859(23)	0.855(33)	0.858(24)	0.843(16)	0.8474(89)	0.852(13)
	2	0.716(16)	0.713(17)	0.713(16)	0.697(20)	0.704(15)	0.718(14)
	3	0.591(33)	0.590(21)	0.595(20)	0.579(26)	0.595(17)	0.613(14)
	4	0.524(18)	0.530(18)	0.531(16)	0.533(19)	0.529(15)	0.531(21)
	5	0.451(17)	0.463(18)	0.467(16)	0.476(17)	0.475(14)	0.479(14)
h_{+}	1	1.638(56)	1.656(49)	1.700(45)	1.590(50)	1.609(42)	1.677(40)
	2	1.387(39)	1.394(32)	1.432(28)	1.357(38)	1.379(30)	1.440(27)
	3	1.166(70)	1.164(54)	1.198(46)	1.113(47)	1.154(36)	1.232(28)
	4	0.991(36)	1.014(28)	1.044(26)	1.010(32)	1.023(25)	1.074(25)
	5	0.876(35)	0.892(26)	0.924(25)	0.905(30)	0.919(24)	0.970(25)
\tilde{h}_{\perp}	1	0.751(31)	0.744(22)	0.750(20)	0.739(18)	0.737(16)	0.743(18)
	2	0.639(32)	0.642(23)	0.646(21)	0.624(19)	0.633(17)	0.649(18)
	3	0.553(34)	0.558(25)	0.565(23)	0.541(31)	0.558(21)	0.578(20)
	4	0.503(41)	0.512(29)	0.517(27)	0.524(24)	0.517(22)	0.526(26)
	5	0.432(57)	0.446(45)	0.454(41)	0.467(37)	0.463(34)	0.485(32)
\tilde{h}_{+}	1	0.762(31)	0.755(22)	0.761(21)	0.754(17)	0.749(15)	0.753(19)
	2	0.656(31)	0.660(23)	0.661(21)	0.644(19)	0.651(16)	0.662(20)
	3	0.567(34)	0.578(26)	0.583(23)	0.559(32)	0.576(23)	0.591(21)
	4	0.525(42)	0.538(29)	0.537(27)	0.547(25)	0.537(22)	0.543(27)
	5	0.456(48)	0.479(38)	0.479(36)	0.496(29)	0.488(28)	0.505(30)

TABLE VIII. Values of the $\Lambda_c \rightarrow N$ form factors extracted for each nucleon momentum and each data set.

-
- [1] M. A. Ivanov, V. E. Lyubovitskij, J. G. Körner, and P. Kroll, “Heavy baryon transitions in a relativistic three quark model,” *Phys. Rev.* **D56** (1997) 348–364, [arXiv:hep-ph/9612463 \[hep-ph\]](#).
- [2] M. Pervin, W. Roberts, and S. Capstick, “Semileptonic decays of heavy Λ baryons in a quark model,” *Phys. Rev.* **C72** (2005) 035201, [arXiv:nucl-th/0503030 \[nucl-th\]](#).
- [3] K. Azizi, M. Bayar, Y. Sarac, and H. Sundu, “Semileptonic $\Lambda_{b,c}$ to Nucleon Transitions in Full QCD at Light Cone,” *Phys. Rev.* **D80** (2009) 096007, [arXiv:0908.1758 \[hep-ph\]](#).
- [4] A. Khodjamirian, C. Klein, T. Mannel, and Y.-M. Wang, “Form Factors and Strong Couplings of Heavy Baryons from QCD Light-Cone Sum Rules,” *JHEP* **09** (2011) 106, [arXiv:1108.2971 \[hep-ph\]](#).
- [5] T. Gutsche, M. A. Ivanov, J. G. Körner, V. E. Lyubovitskij, and P. Santorelli, “Heavy-to-light semileptonic decays of Λ_b and Λ_c baryons in the covariant confined quark model,” *Phys. Rev.* **D90** no. 11, (2014) 114033, [arXiv:1410.6043 \[hep-ph\]](#). [Erratum: *Phys. Rev.*D94,no.5,059902(2016)].
- [6] C.-D. Lü, W. Wang, and F.-S. Yu, “Test flavor SU(3) symmetry in exclusive Λ_c decays,” *Phys. Rev.* **D93** no. 5, (2016) 056008, [arXiv:1601.04241 \[hep-ph\]](#).
- [7] R. N. Faustov and V. O. Galkin, “Semileptonic decays of Λ_c baryons in the relativistic quark model,” *Eur. Phys. J.* **C76** no. 11, (2016) 628, [arXiv:1610.00957 \[hep-ph\]](#).
- [8] C.-F. Li, Y.-L. Liu, K. Liu, C.-Y. Cui, and M.-Q. Huang, “Analysis of the semileptonic decay $\Lambda_c \rightarrow ne^+\nu_e$,” *J. Phys.* **G44** no. 7, (2017) 075006, [arXiv:1610.05418 \[hep-ph\]](#).
- [9] S. de Boer and G. Hiller, “Flavor and new physics opportunities with rare charm decays into leptons,” *Phys. Rev.* **D93** no. 7, (2016) 074001, [arXiv:1510.00311 \[hep-ph\]](#).
- [10] S. Fajfer and N. Košnik, “Prospects of discovering new physics in rare charm decays,” *Eur. Phys. J.* **C75** no. 12, (2015) 567, [arXiv:1510.00965 \[hep-ph\]](#).
- [11] T. Feldmann, B. Müller, and D. Seidel, “ $D \rightarrow \rho \ell^+ \ell^-$ decays in the QCD factorization approach,” *JHEP* **08** (2017) 105, [arXiv:1705.05891 \[hep-ph\]](#).
- [12] **LHCb** Collaboration, R. Aaij *et al.*, “Search for the rare decay $\Lambda_c^+ \rightarrow p \mu^+ \mu^-$,” [arXiv:1712.07938 \[hep-ex\]](#).
- [13] **BaBar** Collaboration, J. P. Lees *et al.*, “Searches for Rare or Forbidden Semileptonic Charm Decays,” *Phys. Rev.* **D84** (2011) 072006, [arXiv:1107.4465 \[hep-ex\]](#).
- [14] **E653** Collaboration, K. Kodama *et al.*, “Upper limits of charm hadron decays to two muons plus hadrons,” *Phys. Lett.* **B345** (1995) 85–92.
- [15] T. Feldmann and M. W. Y. Yip, “Form Factors for $\Lambda_b \rightarrow \Lambda$ Transitions in SCET,” *Phys. Rev.* **D85** (2012) 014035, [arXiv:1111.1844 \[hep-ph\]](#). [Erratum: *Phys. Rev.*D86,079901(2012)].
- [16] Y. Iwasaki and T. Yoshie, “Renormalization group improved action for $SU(3)$ lattice gauge theory and the string tension,” *Phys.Lett.* **B143** (1984) 449.
- [17] D. B. Kaplan, “A Method for simulating chiral fermions on the lattice,” *Phys.Lett.* **B288** (1992) 342–347, [arXiv:hep-lat/9206013](#).
- [18] V. Furman and Y. Shamir, “Axial symmetries in lattice QCD with Kaplan fermions,” *Nucl.Phys.* **B439** (1995) 54–78, [arXiv:hep-lat/9405004](#).
- [19] Y. Shamir, “Chiral fermions from lattice boundaries,” *Nucl.Phys.* **B406** (1993) 90–106, [arXiv:hep-lat/9303005](#).
- [20] Z. S. Brown, W. Detmold, S. Meinel, and K. Orginos, “Charmed bottom baryon spectroscopy from lattice QCD,” *Phys.Rev.* **D90** (2014) 094507, [arXiv:1409.0497 \[hep-lat\]](#).
- [21] **RBC, UKQCD** Collaboration, Y. Aoki *et al.*, “Continuum Limit Physics from 2+1 Flavor Domain Wall QCD,” *Phys. Rev.* **D83** (2011) 074508, [arXiv:1011.0892 \[hep-lat\]](#).
- [22] W. Detmold, C. Lehner, and S. Meinel, “ $\Lambda_b \rightarrow p \ell^- \bar{\nu}_\ell$ and $\Lambda_b \rightarrow \Lambda_c \ell^- \bar{\nu}_\ell$ form factors from lattice QCD with relativistic heavy quarks,” *Phys. Rev.* **D92** no. 3, (2015) 034503, [arXiv:1503.01421 \[hep-lat\]](#).
- [23] S. Meinel, “Bottomonium spectrum at order v^6 from domain-wall lattice QCD: Precise results for hyperfine splittings,” *Phys. Rev.* **D82** (2010) 114502, [arXiv:1007.3966 \[hep-lat\]](#).
- [24] S. Hashimoto, A. X. El-Khadra, A. S. Kronfeld, P. B. Mackenzie, S. M. Ryan, *et al.*, “Lattice QCD calculation of $\bar{B} \rightarrow D \ell \bar{\nu}$ decay form-factors at zero recoil,” *Phys.Rev.* **D61** (1999) 014502, [arXiv:hep-ph/9906376 \[hep-ph\]](#).
- [25] A. X. El-Khadra, A. S. Kronfeld, P. B. Mackenzie, S. M. Ryan, and J. N. Simone, “The Semileptonic decays $B \rightarrow \pi \ell \nu$ and $D \rightarrow \pi \ell \nu$ from lattice QCD,” *Phys.Rev.* **D64** (2001) 014502, [arXiv:hep-ph/0101023 \[hep-ph\]](#).
- [26] C. Lehner, “Automated lattice perturbation theory and relativistic heavy quarks in the Columbia formulation,” *PoS LATTICE2012* (2012) 126, [arXiv:1211.4013 \[hep-lat\]](#).
- [27] C. Lehner. Private communication, 2016.
- [28] W. Detmold and S. Meinel, “ $\Lambda_b \rightarrow \Lambda \ell^+ \ell^-$ form factors, differential branching fraction, and angular observables from lattice QCD with relativistic b quarks,” *Phys. Rev.* **D93** no. 7, (2016) 074501, [arXiv:1602.01399 \[hep-lat\]](#).
- [29] A. X. El-Khadra, A. S. Kronfeld, and P. B. Mackenzie, “Massive fermions in lattice gauge theory,” *Phys. Rev.* **D55** (1997) 3933–3957, [arXiv:hep-lat/9604004 \[hep-lat\]](#).
- [30] **RBC, UKQCD** Collaboration, T. Blum *et al.*, “Domain wall QCD with physical quark masses,” *Phys. Rev.* **D93** no. 7, (2016) 074505, [arXiv:1411.7017 \[hep-lat\]](#).
- [31] S. Meinel, “ $\Lambda_c \rightarrow \Lambda \ell^+ \nu_\ell$ form factors and decay rates from lattice QCD with physical quark masses,” *Phys. Rev. Lett.* **118** no. 8, (2017) 082001, [arXiv:1611.09696 \[hep-lat\]](#).

- [32] C. Bourrely, I. Caprini, and L. Lellouch, “Model-independent description of $B \rightarrow \pi \ell \nu$ decays and a determination of $|V_{ub}|$,” *Phys.Rev.* **D79** (2009) 013008, [arXiv:0807.2722 \[hep-ph\]](#).
- [33] J. A. Bailey *et al.*, “ $B \rightarrow Kl^+l^-$ decay form factors from three-flavor lattice QCD,” *Phys. Rev.* **D93** no. 2, (2016) 025026, [arXiv:1509.06235 \[hep-lat\]](#).
- [34] **Particle Data Group** Collaboration, C. Patrignani *et al.*, “Review of Particle Physics,” *Chin. Phys.* **C40** no. 10, (2016) 100001.
- [35] See Supplemental Material at <https://arxiv.org/src/1712.05783/anc> for files containing the form factor parameter values and covariances.
- [36] **UTfit** Collaboration, “Standard model fit results: Summer 2016.” <http://www.utfit.org/UTfit/ResultsSummer2016SM>.
- [37] **BESIII** Collaboration, M. Ablikim *et al.*, “Measurement of the absolute branching fraction for $\Lambda_c^+ \rightarrow \Lambda e^+ \nu_e$,” *Phys. Rev. Lett.* **115** no. 22, (2015) 221805, [arXiv:1510.02610 \[hep-ex\]](#).
- [38] S. de Boer, B. Müller, and D. Seidel, “Higher-order Wilson coefficients for $c \rightarrow u$ transitions in the standard model,” *JHEP* **08** (2016) 091, [arXiv:1606.05521 \[hep-ph\]](#).
- [39] S. de Boer, *Probing the standard model with rare charm decays*. PhD thesis, Technische Universität Dortmund, 2017. <http://hdl.handle.net/2003/36043>.
- [40] S. de Boer, “Two loop virtual corrections to $b \rightarrow (d, s)\ell^+\ell^-$ and $c \rightarrow u\ell^+\ell^-$ for arbitrary momentum transfer,” *Eur. Phys. J.* **C77** no. 11, (2017) 801, [arXiv:1707.00988 \[hep-ph\]](#).
- [41] S. de Boer. Private communication, 2017.
- [42] K. G. Chetyrkin, J. H. Kühn, and M. Steinhauser, “RunDec: A Mathematica package for running and decoupling of the strong coupling and quark masses,” *Comput. Phys. Commun.* **133** (2000) 43–65, [arXiv:hep-ph/0004189 \[hep-ph\]](#).
- [43] S. Fajfer and S. Prelovsek, “Effects of littlest Higgs model in rare D meson decays,” *Phys. Rev.* **D73** (2006) 054026, [arXiv:hep-ph/0511048 \[hep-ph\]](#).
- [44] P. Böer, T. Feldmann, and D. van Dyk, “Angular Analysis of the Decay $\Lambda_b \rightarrow \Lambda(\rightarrow N\pi)\ell^+\ell^-$,” *JHEP* **01** (2015) 155, [arXiv:1410.2115 \[hep-ph\]](#).
- [45] T. Gutsche, M. A. Ivanov, J. G. Körner, V. E. Lyubovitskij, and P. Santorelli, “Rare baryon decays $\Lambda_b \rightarrow \Lambda l^+l^-$ ($l = e, \mu, \tau$) and $\Lambda_b \rightarrow \Lambda\gamma$: differential and total rates, lepton- and hadron-side forward-backward asymmetries,” *Phys.Rev.* **D87** (2013) 074031, [arXiv:1301.3737 \[hep-ph\]](#).
- [46] D. J. Broadhurst and A. G. Grozin, “Matching QCD and HQET heavy - light currents at two loops and beyond,” *Phys. Rev.* **D52** (1995) 4082–4098, [arXiv:hep-ph/9410240 \[hep-ph\]](#).
- [47] K. Azizi, M. Bayar, Y. Sarac, and H. Sundu, “FCNC transitions of $\Lambda_{b,c}$ to nucleon in SM,” *J. Phys.* **G37** (2010) 115007.
- [48] B. B. Şirvanli, “Search for $c \rightarrow ul^+l^-$ transition in charmed baryon decays,” *Phys. Rev.* **D93** no. 3, (2016) 034027.
- [49] A. Paul, I. I. Bigi, and S. Recksiegel, “On $D \rightarrow X_u l^+l^-$ within the Standard Model and Frameworks like the Littlest Higgs Model with T Parity,” *Phys. Rev.* **D83** (2011) 114006, [arXiv:1101.6053 \[hep-ph\]](#).
- [50] **SciDAC, LHPC, UKQCD** Collaboration, R. G. Edwards and B. Joo, “The Chroma software system for lattice QCD,” *Nucl.Phys.Proc.Suppl.* **140** (2005) 832, [arXiv:hep-lat/0409003 \[hep-lat\]](#).